Original Research Article

Institution of MECHANICAL ENGINEERS

Journal of NANOMATERIALS NANOENGINEERING AND NANOSYSTEMS

Proc IMechE Part N:
J Nanomaterials, Nanoengineering and Nanosystems
1–23

DOI: 10.1177/23977914241304066
journals.sagepub.com/home/pin
Sage

Insights using Hamilton-Crosser model in Williamson hybrid nanofluids with homogeneous-heterogeneous reactions and diagonal electromagnetic effects

Neelav Sarma, Bhagyashri Patgiri and Ashish Paul

Abstract

The study of Carboxymethyl Cellulose (CMC)-based Williamson hybrid nanofluids offers a significant leap in fluid dynamics and thermal management systems. This research investigates the flow characteristics over a porous, horizontally stretched cylindrical surface, incorporating complex phenomena such as Hall current, ion slip, diagonal magnetic fields, suction, velocity slip and thermal slip. A unique aspect is the inclusion of uniform and exponentially space-dependent heat sources, critical for advanced thermal transport processes. Using the Hamilton-Crosser model for accurate thermophysical properties and the Runge-Kutta-Fehlberg method for numerical analysis, the study examines the impact of varying hybrid nanoparticle concentrations (4% to 20%) on flow behaviour. The findings reveal that nanoparticles enhance viscosity, significantly increasing skin friction and momentum transfer, even as factors like the Weissenberg number, Hall current and ion slip mitigate these effects. The study emphasises the thermal management advantages of Carboxymethyl Cellulose-based Williamson hybrid nanofluids, especially when heat sources and homogeneous-heterogeneous reactions are involved. Notable differences are observed between pure Carboxymethyl Cellulose-based Williamson fluids and their hybrid nanofluid counterparts, particularly in velocity, temperature distribution and reaction dynamics. These results are promising for practical applications such as magnetic drug targeting, porous heat exchangers, magnetohydrodynamic systems and electronic cooling. The research underscores the potential of Carboxymethyl Cellulose-based Williamson hybrid nanofluids to enhance energy efficiency and reliability in industrial processes, making them pivotal for future developments in heat management technologies.

Keywords

Hall current and ion slip, suction, velocity slip, thermal slip, exponential heat source

Date received: 19 June 2024; accepted: 15 November 2024

Introduction

The dynamics of non-Newtonian fluids have garnered substantial interest due to their numerous natural and industrial applications. The relationship between the stress tensor and the deformation rate tensor in non-Newtonian fluids is nonlinear, leading to intricate nonlinear equations. The complexities involved in solving these nonlinear or higher-order differential equations fuel ongoing research interest. Notably, many physiological fluids, such as blood, deviate from Newtonian behaviour, prompting the development of several non-Newtonian models to investigate fluid dynamics within biological systems. Among these models, the Williamson model[1] is particularly effective in describing the properties of physiological fluids. This model is inherently nonlinear and can be simplified to the Newtonian fluid model under certain conditions. In the Williamson model, apparent viscosity transitions smoothly from μ_0 at zero shear rates to μ_∞ as the shear rate increases indefinitely. This gradual change in viscosity accurately reflects the behaviour of many physiological and industrial fluids. Nadeem and Akram[2]

Department of Mathematics, Cotton University, Guwahati, AS, India

Corresponding author:
Neelav Sarma, Department of Mathematics, The Assam Royal Global University, Guwahati, Assam, 781035, India.
Email: mth2091006_neelav@cottonuniversity.ac.in

investigated the peristaltic motion of a Williamson model within an asymmetric conduit. Iqbal et al.[3] conducted a numerical investigation of the flow behaviour of a Williamson fluid over a cylinder undergoing exponential stretching. Rashid et al.[4] studied how the magnetic field induced by peristaltic motion affects the behaviour of an incompressible Williamson fluid within a curved channel. Loganathan and Dhivya[5] investigated the boundary layer motion of a Williamson fluid around a permeable cylinder using the Crank-Nicolson method. Some recent studies on Williamson fluid have been conducted by Shah et al.,[6] Sharma and Jain,[7] Gangadhar et al.,[8] Zaman et al.,[9] Akbar et al.,[10] and Kulkarni and Shankar.[11]

The unyielding pursuit of optimal heat transfer solutions across diverse domains such as electronics, power generation and medical sciences has catalysed continuous evolution. Although nanofluids marked a pivotal advancement, the quest for greater efficiency spurred the advent of hybrid nanofluids in the late 1990s and early 2000s, heralding a paradigmatic shift in fluid engineering. The driving impetus behind hybrid nanofluids was to transcend the limitations of conventional NFs by harnessing synergistic interactions between multiple types of nanoparticles immersed within a base fluid. This strategic amalgamation not only aims to exploit the unique properties inherent to individual nanoparticles but also seeks to synergistically enhance the overall thermal and physical characteristics of the composite fluid. Akram and Akbar[12] explored the electroosmotic propulsion of peristaltic and ciliary flows in a mixture of propylene glycol and water, transporting titania nanoparticles. Ghadikolaei et al.[13] studied MHD flow and heat transfer characteristics involving an incompressible micropolar dusty fluid with carbon nanotube (CNT)-water nanoparticles over-stretching plate.

Consequently, hybrid nanofluids represent a bespoke approach where the blending of diverse nanoparticles with base fluids yields a multifunctional material capable of outperforming its constituent elements or conventional nanofluids alone. Turcu et al.[14] were pioneers in creating the initial hybrid nanofluid using polypyrrole and multiwall carbon nanotubes. Recently, there has been a surge in scholarly articles dedicated to hybrid nanofluids research. Ranga Babu et al.[15] provided a comprehensive review discussing methodologies to assess and enhance the stability of hybrid nanofluids. Suresh et al.[16] fabricated a composite of aluminium oxide and copper through a method involving hydrogen reduction. Zainal et al.[17] developed hybrid nanofluids employing aluminium and copper oxides, observing reduced skin friction and local Nusselt numbers in buoyant opposing flow conditions. Ghadikolaei et al.[18] researched the thermal and physical properties of a TiO2–Cu/H2O hybrid nanofluid, focussing on how the shape factor influences its behaviour in a magnetohydrodynamic stagnation point flow. Adnan et al.[19] introduced a novel subclass of nanofluids, tetra-hybrid nanofluids and proposed a new theoretical framework for predicting heat transfer characteristics. Zubair et al.[20] investigated the dynamics of thermal energy in the context of the rheological properties of a Williamson hybrid nanofluid on a surface in rotational motion. Akbar et al.[21] explored the electroosmotic behaviour of a thermally layered micropolar nanofluid flow involving copper and silver nanoparticles within a microchannel in the context of biological interactions. Ghadikolaei et al.[22] studied natural convection heat transfer characteristics in an MHD non-Newtonian Carreau hybrid nanofluid surrounding a rotating cone. Their research considered the influences of nonlinear thermal radiation, variable thermal conductivity, heat generation or absorption and different nanoparticle geometries. Paul et al.,[23] Guo et al.,[24,25] Akbar et al.,[26,27] and Ghadikolaei and Gholinia,[28,29] Ghadikolaei et al.,[30] Fadhel et al.[31] conducted some relevant impactful research using hybrid nanofluid recently.

Homogeneous-heterogeneous reactions are at the forefront of MHD research using nanofluids or hybrid nanofluids and constitute an important field of study in fluid dynamics. These reactions are complex processes in which chemical interactions occur between species in distinct phases, significantly altering the fluid's temperature and flow parameters. In MHD systems containing nanofluids, the interaction of magnetic fields with nanoparticles complicates these processes by changing reaction rates and energy transfer mechanisms. Chaudhary and Merkin[32] investigated a model concerning boundary-layer flow with both homogeneous and heterogeneous reactions, by incorporating the impacts of diminishing autocatalysis. Khan et al.[33] examined a variant of reactions blending uniform and diverse characteristics within MHD stagnation flow, incorporating effects such as viscous dissipation and Joule heating. Hussain et al.[34] present a study contrasting the convective flow of Williamson fluid around both a cylindrical object and a flat sheet, investigating reactions that vary in uniformity. Ramzan et al.[35] investigated the impact of MHD reactions, which combine homogeneous and heterogeneous characteristics, on the flow of a third-grade fluid accompanied by Cattaneo-Christov heat flux. He et al.[36] investigated the effects of time-periodic boundary conditions on unsteady MHD flow in a rotating annular region, incorporating homogeneous-heterogeneous chemical reactions in Walters' B fluids. Nandkeolyar et al.,[37] Tanveer et al.,[38] Pooja et al.,[39] Ramzan et al.,[40] and Noor[41] shared some salient information through their research in this domain.

Following a thorough review of existing research, it is apparent that no prior research has examined the flow of CMC-based Williamson hybrid nanofluid across a porous, horizontally stretched cylindrical geometry, particularly considering the combined effects of Hall current, ion slip, diagonal magnetic field ($\xi = 45°$),

suction, velocity slip and thermal slip. The utilisation of hybrid nanoparticles in this study leverages their emergent properties, derived from the concerted interaction of distinct material components, to yield enhanced thermal conductivity, stability and fluid dynamical characteristics. This hybrid approach facilitates superior heat transfer and rheological performance by circumventing the constraints inherent to single-component nanoparticles, culminating in optimised thermophysical properties. This study's uniqueness is further enhanced by incorporating uniform and exponential space-dependent heat sources. CMC is utilised as a base for Williamson hybrid nanofluid because of its shear-thinning behaviour, making it an ideal choice to mimic non-Newtonian fluids with viscosity decreasing under shear, which matches the properties of Williamson fluid. The present study utilises the Hamilton-Crosser model[42] for computation purposes, making it distinctive from other nanofluid models in the available literature. Additionally, the influence of a homogeneous-heterogeneous reaction mechanism is analysed to highlight the significance and impact of these phenomena. This investigation also focuses on the computational analysis of skin friction and local Nusselt numbers with varying concentrations (4%, 8%, 12%, 16%, 20%) of Williamson hybrid nanofluid. It provides a graphical comparison of the parametric effects between CMC-based Williamson hybrid nanofluid and Williamson fluid. The primary objective of this research is to address the following critical questions:

- How do Hall current and ion slip impact the velocity, temperature and homogeneous-heterogeneous reaction profiles?
- How do uniform and exponential space-dependent heat sources influence the temperature profile?
- What are the effects of various parameters, such as magnetic field, porosity, suction and slip, on the homogeneous-heterogeneous reaction profile?
- How do the velocity, temperature and homogeneous-heterogeneous reaction profiles vary between Williamson fluid and CMC-based Williamson hybrid nanofluid under different parameters?
- How are the skin friction and local Nusselt number affected by different parameters with varying concentrations of hybrid nanofluid?
- How do the skin friction coefficient and local Nusselt number for CMC-based Williamson hybrid nanofluid compare to Williamson fluid at different nanoparticle concentrations?

Mathematical formulation

Williamson fluid model

The constitutive relationship within the Williamson framework is mathematically expressed as follows:

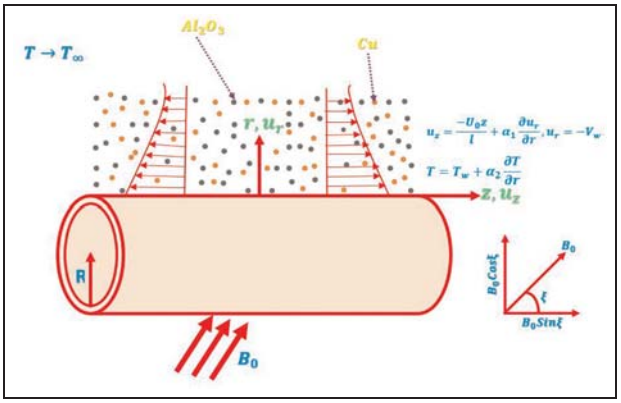

Figure 1. Illustrative depiction of the flow.

$$\tau_0 = -p\mathbf{I} + \tau_e \tag{1}$$

Here, p is pressure, $\mathbf{I}$ is identity vector, τ_e is the extra stress.

Now,

$$\tau_e = [\mu_\infty + (1 - \Gamma\gamma^*)^{-1}(\mu_{hnf} - \mu_\infty)]\boldsymbol{\alpha}_1 \tag{2}$$

where, $\Gamma(>0)$ is the positive time constant, μ_{hnf} is the viscosity at zero rates of shear stress, μ_∞ is the viscosity at infinite shear stress, γ^* is defined as:

$$\gamma^* = \sqrt{0.5\Pi}, \text{ where } \Pi = 0.5\ trace\ (\boldsymbol{\alpha}_1^2) \tag{3}$$

In this analysis, we specifically examine the scenario where $\mu_\infty = 0$ and $\Gamma\gamma^* < 1$. Consequently,

$$\tau_e = [(1 - \Gamma\gamma^*)^{-1}\mu_{hnf}]\boldsymbol{\alpha}_1 \tag{4}$$

Utilising the binomial theorem on equation (4) yields the subsequent formulation,

$$\tau_e = \mu_{hnf}[1 + \Gamma\gamma^*]\boldsymbol{\alpha}_1 \tag{5}$$

which represents the extra stress used in this model.

Geometric model and equations involved

The mathematical model addresses a steady, two-dimensional, laminar, incompressible, axisymmetric MHD flow of a Carboxymethyl Cellulose-based Williamson hybrid nanofluid containing $Al_2O_3 - Cu$ nanoparticles over a horizontally porous, stretching cylinder. The study investigates the transport of solutal energy through homogeneous and heterogeneous chemical species. Thermal energy transport is analysed, accounting for viscous dissipation and Joule heating. The cylinder is assumed to be porous, allowing fluid to either be injected or withdrawn through its surface, influencing the boundary layer thickness and flow

dynamics. In Figure 1, the cylindrical coordinate system places the z-axis along the cylinder and the r-axis perpendicular to its surface. The z-axis represents the longitudinal direction of the flow, while the r-axis corresponds to the radial direction, capturing the variation of velocity and temperature across the boundary layer. The axisymmetry of the problem simplifies the analysis by assuming no variation in the azimuthal direction, thus reducing the three-dimensional problem to a two-dimensional form. The fluid velocity is defined as $u_z = U_w = \frac{zU_0}{l}$, where $U_0 > 0$ and l represents the cylinder's length. This velocity profile describes a linearly stretching surface, where the stretching rate increases along the length of the cylinder, intensifying the flow near the surface. A magnetic field B_0 is applied a to the cylinder's surface at a 45° angle This oblique magnetic field introduces axial and radial components of the Lorentz force, altering the flow and heat transfer patterns compared to a purely vertical or horizontal field application. The temperature of the cylinder is T_w, with the ambient temperature being T_∞. Including uniform and exponential heat sources in the energy equation significantly impacts heat transfer phenomena. The exponential heat source is particularly relevant in capturing localised heating effects, whereas the uniform heat source represents a consistent thermal input across the domain. The model also considers the effects of velocity slip, thermal slip and suction.

In accordance with the previous assumptions and using boundary layer theory, the mathematical representation for the flow is as follows (Ref. Khan et al.,[43] Veera Krishna[44]):

Equation of continuity. For incompressible and steady flow, the continuity equation in vector notation is expressed as $\nabla \mathbf{q}^* = 0$. Here, the velocity vector $\mathbf{q}^*$ comprises components (u_r, u_θ, u_z) corresponding to the radial, azimuthal and axial directions (r, θ, z), respectively. The differential operator ∇ is defined as $\frac{\partial}{\partial r} + \left(\frac{1}{r}\right)\frac{\partial}{\partial \theta} + \frac{\partial}{\partial z}$. In this study, our focus is limited to the radial and transverse velocity components along the r and z axes, denoted as u_r and u_z, respectively. Consequently, the continuity equation simplifies to:

$$\frac{\partial (ru_r)}{\partial r} + \frac{\partial (ru_z)}{\partial z} = 0 \tag{6}$$

Momentum conservation equation. In the context of steady fluid flow, the momentum equation is represented in vector notation as

$$\rho_{hnf}((\mathbf{q}^*.\nabla)\mathbf{q}^*) = -\nabla p + \nabla \tau_0 + \sigma_{hnf}\overrightarrow{B_0}\mathbf{J}_0 Sin^2\xi - \frac{\mu_{hnf}}{k}\mathbf{q}^* \tag{7}$$

where ρ is density, μ is dynamic viscosity, σ is electrical conductivity, τ_0 is Cauchy stress tensor, B_0 is external magnetic field, k is the permeability of the medium.

When the magnetic field's intensity is significantly high, the generalised Ohm's law is adjusted to account for Hall and ion-slip effects, as

$$\mathbf{J_i} = (\mathbf{E_i} + \mathbf{V_i}\times\mathbf{B_i}) - \frac{\omega_c\tau_c}{B_0}(\mathbf{J_i}\times\mathbf{B_i}) + \frac{\omega_c\tau_c\beta_1}{B_0^2}((\mathbf{J_i}\times\mathbf{B_i})\times\mathbf{B_i}) \tag{7a}$$

By assuming $\omega_c\tau_c \sim O(1)$ and $\omega_i\tau_i \ll 1$ in equation (7a) and setting $\mathbf{E_i} = 0$, equation (7a) simplifies to:

$$\mathbf{J}_0 = B_0\frac{H_c}{\left(H_c^2 + (1 + H_cH_i)^2\right)} \tag{7b}$$

where, $H_c = \omega_c\tau_c$ and $H_i = \omega_i\tau_i$

In the present flow model, constant pressure is presupposed. By incorporating the τ_0 formulation from Williamson's model and using (7b), we derive the subsequent equation in cylindrical coordinates:

$$u_r\frac{\partial u_r}{\partial r} + u_z\frac{\partial u_z}{\partial z} = \nu_{hnf}\left(\frac{1}{r}\frac{\partial u_z}{\partial r} + \frac{\partial^2 u_z}{\partial r^2} + \frac{\Gamma}{\sqrt{2}r}\left(\frac{\partial u_z}{\partial r}\right)^2 + \sqrt{2}\Gamma\frac{\partial u_z}{\partial r}\frac{\partial^2 u_z}{\partial r^2}\right) - \frac{\sigma_{hnf}B_0^2H_cu_z}{\left(H_c^2 + (1 + H_cH_i)^2\right)}Sin^2\xi - \nu_{hnf}\frac{u_z}{k} \tag{8}$$

where Γ is Williamson's fluid parameter.

Energy conservation equation. In the realm of steady, incompressible Williamson hybrid nanofluid dynamics, the constitutive energy equation is conceptualised as

$$(\rho C_p)_{hnf}(\mathbf{q}^*.\nabla)T = \nabla.(K_{hnf}\nabla T) + Q_u(T - T_\infty) + Q_0\mathbf{q}^* \tag{9}$$

where $Q_0 = Q_e(T_w - T_\infty)\exp\left(n\left(\frac{-l}{\nu_f}\right)^{0.5}\right)$ is the exponential space-dependant heat source parameter. Here, $\exp\left(n\left(\frac{-l}{\nu_f}\right)^{0.5}\right)$ depicts exponential decay, which describes how the temperature variation due to the heat source diminishes or spreads relative to the specified parameters. Q_u is the uniform heat source, K is the thermal conductivity, ρC_p is specific heat capacity.

Thus, the energy equation takes the form in cylindrical coordinates:

$$u_r\frac{\partial T}{\partial r} + u_z\frac{\partial T}{\partial z} = \alpha_{hnf}\left(\frac{1}{r}\frac{\partial T}{\partial r} + \frac{\partial^2 T}{\partial r^2}\right) + \frac{\sigma_{hnf}B_0^2u_z^2}{(\rho C_p)_{hnf}\left(H_c^2 + (1 + H_cH_i)^2\right)}Sin^2\xi + \frac{Q_u}{(\rho C_p)_{hnf}}(T - T_\infty) + \frac{Q_e}{(\rho C_p)_{hnf}}(T_w - T_\infty)\exp\left(\left(\frac{-l}{\nu_f}\right)^{0.5}nz\right) \quad (10)$$

Homogeneous-heterogeneous reactions. The homogeneous reaction is characterised by cubic autocatalysis, a specific type of reaction mechanism where the product of the reaction also acts as a catalyst. The reaction can be described as follows:

$$\alpha_c + 2\beta_c \rightarrow 3\beta_c \quad (11)$$

This implies that one molecule of α_c reacts with two molecules of β_c to form three molecules of β_c. The rate of this reaction, denoted by R_{hom}, is given by:

$$R_{hom} = K_cAB^2 \quad (12)$$

Here, A, B is the concentration of species α_c, β_c, respectively and K_c is the rate constant for the homogeneous reaction.

In this cubic autocatalytic reaction, the term B^2 indicates that the reaction rate is proportional to the square of the concentration of species β_c, making it a second-order reaction with respect to β_c.

Simultaneously, the species α_c and β_c undergo a heterogeneous reaction on the surface of a catalyst. The reaction can be represented as:

$$\alpha_c \rightarrow \beta_c \quad (13)$$

In this scenario, a molecule of α_c is converted to a molecule of β_c on the catalyst surface. The rate of this heterogeneous reaction, denoted by R_{het}, is expressed as:

$$R_{het} = K_sA \quad (14)$$

A is the concentration of species α_c and K_s is the rate constant for the homogeneous reaction.

In a system with both homogeneous and heterogeneous processes, the interaction of the two reaction rates influences the overall dynamics. The homogeneous cubic autocatalytic process rapidly increases the concentration of β_c, whereas the heterogeneous reaction gradually converts α_c to β_c.

These reactions must be integrated into the governing equations for species transport and reaction kinetics in fluid flow, which are commonly represented by the convection-diffusion-reaction equations in vector form:

For species α_c:

$$(\mathbf{q}^*.\nabla)A = \nabla.\left(D_{Ahnf}\nabla A\right) - K_cAB^2 - SK_sB \quad (15)$$

For species β_c:

$$(\mathbf{q}^*.\nabla)B = \nabla.\left(D_{Bhnf}\nabla B\right) + K_cAB^2 + SK_sB \quad (16)$$

D_A and D_B are the diffusion coefficients for species α_c and β_c, respectively.

In cylindrical coordinates, these equations take the form:

$$u_r\frac{\partial A}{\partial r} + u_z\frac{\partial A}{\partial z} = D_{A_{hnf}}\left(\frac{1}{r}\frac{\partial A}{\partial r} + \frac{\partial^2 A}{\partial r^2}\right) - K_rAB^2 - SK_sA \quad (17)$$

$$u_r\frac{\partial B}{\partial r} + u_z\frac{\partial B}{\partial z} = D_{B_{hnf}}\left(\frac{1}{r}\frac{\partial B}{\partial r} + \frac{\partial^2 B}{\partial r^2}\right) + K_rAB^2 + SK_sA \quad (18)$$

With suitable boundary constraints

$$\left.\begin{aligned} u_z = \frac{-U_0z}{l} + \alpha_1\frac{\partial u_r}{\partial r}, u_r = -V_w, T = T_w + \alpha_2\frac{\partial T}{\partial r}, \\ \frac{\partial A}{\partial r} = \frac{K_sA}{D_A}, \frac{\partial B}{\partial r} = \frac{K_sA}{D_B} \text{ at } r = R \\ u_z \rightarrow 0, T \rightarrow T_\infty, A \rightarrow A_0, B \rightarrow 0 \text{ at } r \rightarrow \infty \end{aligned}\right\} \quad (19)$$

At the surface of the cylinder ($r = R$), the axial velocity $u_z = \frac{-U_0z}{l} + \alpha_1\frac{\partial u_r}{\partial r}$ describes the velocity along the z-axis. Here, $\frac{-U_0z}{l}$ represents the stretching velocity of the cylinder, while $\alpha_1\frac{\partial u_r}{\partial r}$ accounts for the velocity slip effect, where α_1 is the velocity slip coefficient and $\frac{\partial u_r}{\partial r}$ is the radial velocity gradient which allows for non-zero tangential velocity at the surface with slip-flow regimes. Radial velocity component $u_r = -V_w$ represents the wall suction or injection velocity which affects the thickness of the boundary layer and influences the transport of momentum and heat. Temperature condition $T = T_w + \alpha_2\frac{\partial T}{\partial r}$ imposes a thermal slip at the surface, accounting for partial accommodation of thermal energy between the fluid and the cylinder surface, allowing for temperature discontinuities typical in non-equilibrium thermal boundary layers. Concentration of species $\frac{\partial A}{\partial r} = \frac{K_sA}{D_A}, \frac{\partial B}{\partial r} = \frac{K_sA}{D_B}$ define the flux of species A and B at the surface.

At the far-field condition ($r \rightarrow \infty$), axial velocity $u_z \rightarrow 0$ specifies that the fluid velocity approaches zero as the radial distance increases, ensuring no flow far from the surface. Temperature $T \rightarrow T_\infty$ sets the temperature to approach the ambient value T_∞, signifying thermal equilibrium far from the surface. Concentration

of species $A \to A_0, B \to 0$ indicate that species A reaches its far-field concentration A_0, species B vanishes as no more species B exists far from the surface due to the localised reaction near the cylinder.

Similarity analysis and dimensionless parameters. The similarity transformation utilised (Refs. Khan et al.,[43] Alarabi et al.[45]) are:

$$\left.\begin{array}{l} u_z = \frac{U_0 z}{l} F'(\zeta), u_r = \frac{-R}{r}\sqrt{\frac{U_0 \nu_f}{l}} F(\zeta), \zeta = \frac{r^2 - R^2}{2R}\sqrt{\frac{U_0}{\nu_f l}} \\ \theta(\zeta) = \frac{T - T_\infty}{T_w - T_\infty}, \phi(\zeta) = \frac{A}{A_0}, \psi(\zeta) = \frac{B}{A_0} \end{array}\right\} \tag{20}$$

By utilising (20), equations (8), (10), (17), (18) and (19) can be converted into the following system of coupled nonlinear ordinary differential equations as follows:

$$\begin{aligned} &\frac{1}{C_1 C_2}(2\gamma F'' + (1 + 2\gamma\zeta)F''' + We(1 + 2\gamma\zeta)^{\frac{3}{2}} F'' F''' \\ &\quad + 3We\gamma\left((1 + 2\gamma\zeta)^{\frac{1}{2}} F''^2\right) + \left(FF'' - F'^2\right) \\ &\quad - \frac{C_3}{C_2}\frac{M(1 + H_c H_i)}{\left(H_c^2 + (1 + H_c H_i)^2\right)} F' Sin^2\xi \\ &\quad - \frac{1}{C_1 C_2} k_p F' = 0 \end{aligned} \tag{21}$$

$$\begin{aligned} &\frac{C_4}{C_5}\left((1 + 2\gamma\zeta)\theta'' + 2\gamma\theta'\right) + \Pr F\theta' \\ &\quad + \frac{C_3}{C_5}\Pr Ec\frac{M(1 + H_c H_i)}{\left(H_c^2 + (1 + H_c H_i)^2\right)} F'^2 Sin^2\xi \\ &\quad + \frac{1}{C_5}\Pr(S_1\theta + S_2\exp(-n\zeta)) = 0 \end{aligned} \tag{22}$$

$$\frac{C_6}{Sc}\left((1 + 2\gamma\zeta)\phi'' + 2\gamma\phi'\right) + F\phi' - K_c\phi\psi^2 - K_{vs}\phi = 0 \tag{23}$$

$$\frac{C_6\beta^*}{Sc}\left((1 + 2\gamma\zeta)\psi'' + 2\gamma\psi'\right) + F\psi' + K_c\phi\psi^2 + K_{vs}\phi = 0 \tag{24}$$

With boundary constraints

$$\left.\begin{array}{l} F(\zeta) = S_u, F'(\zeta) - \delta_1 F''(\zeta) = 1, \theta(\zeta) - \delta_2\theta'(\zeta) = 1, \\ \delta_3\phi(\zeta) = \phi'(\zeta), \beta^*\psi'(\zeta) = \delta_3\phi(\zeta) \text{ at } \zeta = 0 \\ F'(\zeta) \to 0, \theta(\zeta) \to 0, \phi(\zeta) \to 1, \psi(\zeta) \to 0 \text{ at } \zeta \to \infty \end{array}\right\} \tag{25}$$

Diffusion equivalence and boundary conditions in homogeneous-heterogeneous reactions. In this section, the scenario assumes equal diffusion coefficients for two chemical species, denoted as D_A and D_B. This equivalence implies a unity ratio of the diffusion parameters that is, $\frac{D_A}{D_B} = 1$. Consequently, the relationship between the dimensionless concentrations of the two species is expressed as:

$$\psi(\zeta) + \phi(\zeta) = 1 \tag{26}$$

By incorporating the diffusion equivalence into the governing equations, the following coupled nonlinear ordinary differential equation is derived:

$$\begin{aligned} &\frac{C_6}{Sc}\left((1 + 2\gamma\zeta)\phi'' + 2\gamma\phi'\right) + F\phi' \\ &\quad - \left(K_c(\phi - 1)^2 + K_{vs}\right)\phi = 0 \end{aligned} \tag{27}$$

Subject to boundary constraints

$$\left.\begin{array}{l} \phi'(\zeta) = \delta_3\phi(\zeta) \text{ at } \zeta = 0 \\ \phi(\zeta) \to 1 \text{ at } \zeta \to \infty \end{array}\right\} \tag{28}$$

This equation elegantly captures the balance of diffusion, convection and reaction dynamics, seamlessly incorporating the impacts of both homogeneous and heterogeneous reactions.

The thermophysical properties used here are based on the Hamilton-Crosser model,[46,47] given by:

$$C_1 = \frac{\mu_f}{\mu_{hnf}} = \left(1 - \varphi_{Al_2O_3}\right)^{\frac{5}{2}}(1 - \varphi_{Cu})^{\frac{5}{2}};$$

$$\begin{aligned} C_2 = \frac{\rho_{hnf}}{\rho_f} &= (1 - \varphi_{Cu})\left(\left(1 - \varphi_{Al_2O_3}\right) + \varphi_{Al_2O_3}\left(\frac{\rho_{Al_2O_3}}{\rho_{CMC}}\right)\right) \\ &\quad + \varphi_{Cu}\rho_{Cu}; \end{aligned}$$

$C_3 = \frac{\sigma_{hnf}}{\sigma_f}$, where

$$\begin{aligned} \frac{\sigma_{hnf}}{\sigma_{nf}} &= \frac{\sigma_{Cu} + 2\sigma_{nf} - 2\varphi_{Cu}(\sigma_{nf} - \sigma_{Cu})}{\sigma_{Cu} + 2\sigma_{nf} + \varphi_{Cu}(\sigma_{nf} - \sigma_{Cu})}, \frac{\sigma_{nf}}{\sigma_f} \\ &= \frac{\sigma_{Al_2O_3} + 2\sigma_{CMC} - 2\varphi_{Al_2O_3}(\sigma_{CMC} - \sigma_{Al_2O_3})}{\sigma_{Al_2O_3} + 2\sigma_{CMC} + \varphi_{Al_2O_3}(\sigma_{CMC} - \sigma_{Al_2O_3})}; \end{aligned}$$

$C_4 = \frac{K_{hnf}}{K_f}$, where

$$\begin{aligned} \frac{K_{hnf}}{K_{nf}} &= \frac{K_{Cu} + 2K_{nf} - 2\varphi_{Cu}(K_{nf} - K_{Cu})}{K_{Cu} + 2K_{nf} + \varphi_{Cu}(K_{nf} - K_{Cu})}, \frac{K_{nf}}{K_f} \\ &= \frac{K_{Al_2O_3} + 2K_{CMC} - 2\varphi_{Al_2O_3}(K_{CMC} - K_{Al_2O_3})}{K_{Al_2O_3} + 2K_{CMC} + \varphi_{Al_2O_3}(K_{CMC} - K_{Al_2O_3})}; \end{aligned}$$

$$C_5 = \frac{(\rho C_p)_{hnf}}{(\rho C_p)_f}, \text{ where } \varphi_{Cu}(\rho C_p)_{Cu} + (1-\varphi_{Cu})(\rho C_p)_{CMC}\left\{\varphi_{Al_2O_3}\frac{(\rho C_p)_{Al_2O_3}}{(\rho C_p)_{CMC}} + (1-\varphi_{Al_2O_3})\right\};$$

$$C_6 = \frac{D_{hnf}}{D_f} = (1-\varphi_{Al_2O_3})(1-\varphi_{Cu})$$

The non-dimensionless parameters involved are:

$$\gamma = \frac{1}{R}\sqrt{\frac{\nu_f l}{U_0}}; M = \frac{B_0^2 l\sigma_f}{U_O\rho_f}; S_1 = \frac{Q_u}{(\rho C_p)_f l};$$

$$k_p = \frac{\nu_f l}{U_0 k}; We = \frac{\Gamma U_0^{\frac{3}{2}} z}{\sqrt{2}\nu_f l^{\frac{3}{2}}}; \Pr = \frac{\nu_f}{\alpha_f}; Sc = \frac{\nu_f}{D_A};$$

$$S_2 = \frac{Q_e}{(\rho C_p)_f l}; Ec = \frac{U_w^2}{(C_p)_f(T_w - T_\infty)}; \beta^* = \frac{D_B}{D_A};$$

$$K_c = \frac{K_r A_0^2 l}{U_0}; \delta_1 = \alpha_1\left(\frac{U_0}{l\nu_f}\right)^{\frac{1}{2}}; \delta_2 = \alpha_2\left(\frac{U_0}{l\nu_f}\right)^{\frac{1}{2}};$$

$$S_u = V_w\left(\frac{l}{U_0\nu_f}\right)^{\frac{1}{2}} > 0; \delta_3 = \frac{K_s}{D_A}\left(\frac{l\nu_f}{U_0}\right)^{\frac{1}{2}}$$

Denotes curvature parameter, magnetic parameter, thermal-dependent heat source parameter, porosity parameter, Weissenberg number, Prandtl number, Schmidt number, exponential space-dependent heat source parameter, Eckert number, ratio of diffusion coefficient, strength of homogeneous-heterogeneous reaction, velocity slip, thermal slip, suction parameter, homogeneous-heterogeneous reaction parameter; respectively. Here, H_c, H_i, K_{vs}, n denote Hall current parameter, ion-slip current parameter, the strength of homogeneous-heterogeneous reaction due to slip and exponential index, respectively.

Thermophysical properties of $CMC - Water, Al_2O_3$ & Cu are given in Table 1.

Table 1. Thermophysical properties.[48–50]

Thermophysical properties	CMC − Water	Al_2O_3	Cu
C_p	4179	765	385
ρ	997.1	3970	8933
K	0.613	40	400
σ	5.5×10^{-6}	35×10^{6}	59.6×10^{6}

Skin friction and local Nusselt number. In this flow problem, the critical engineering parameters include the skin friction coefficient and the local Nusselt number. These parameters act as physical markers, revealing the tangential stress and the rate of thermal transport at the cylindrical surface.

The pertinent expressions for the skin friction coefficient and the local Nusselt number are presented as follows:

$$C_F = \frac{\tau_{rz}}{\frac{1}{2}\rho_f U_w^2}; Nu = \frac{-zq_e}{K_f(T_w - T_\infty)} \tag{29}$$

where

$$\left.\begin{aligned}\tau_{rz} &= \mu_{hnf}\left(\frac{\partial v_z}{\partial r} + \frac{\Gamma}{\sqrt{2}r}\left(\frac{\partial v_z}{\partial r}\right)^2\right)\Big|_{r=R}\\ q_e &= -K_{hnf}\left(\frac{\partial T}{\partial r}\right)_{r=R}\end{aligned}\right\} \tag{30}$$

Using (20) in (29), (30), we get

$$C_F Re^{\frac{1}{2}} = \frac{2}{C_1}\left[F''(0) + \frac{We}{\sqrt{2}}F''^2(0)\right] \tag{31}$$

$$NuRe^{-\frac{1}{2}} = -C_4\theta'(0) \tag{32}$$

Here, $Re = \frac{U_0 z^2}{\nu_f l}$ is local Reynold's number.

Methodology

Equations (21), (22) and (27) are complex, nonlinear ordinary differential equations with boundary conditions (25)–(28). These equations are solved using the shooting method in combination with the Runge-Kutta-Fehlberg algorithm, considering various values of the non-dimensionless parameters. Calculations are performed using MATLAB software. The Runge-Kutta-Fehlberg method is specifically designed for initial value problems, necessitating a reformulation of equations (21), (22) and (27) to fit this method, as

$$F''' = \frac{C_1C_2\left(F'^2 - FF''\right) + C_1C_3\frac{M(1+H_cH_i)}{\left(H_c^2+(1+H_cH_i)^2\right)}F'Sin^2\xi + k_pF' - 2\gamma F'' - 3We\gamma(1+2\gamma\zeta)^{\frac{1}{2}}F''^2}{(1+2\gamma\zeta) + We(1+2\gamma\zeta)^{\frac{3}{2}}F''} \tag{33}$$

$$\theta'' = \frac{-(2\gamma\theta' + \Pr Ec\frac{C_3}{C_4}\frac{M(1+H_cH_i)}{\left(H_c^2+(1+H_cH_i)^2\right)}F'^2Sin^2\xi + \frac{1}{C_4}\Pr S_1\theta + \frac{1}{C_4}\Pr S_2\exp(-n\zeta) + \frac{C_5}{C_4}\Pr F\theta'}{(1+2\gamma\zeta)} \tag{34}$$

$$\phi'' = \frac{Sc\left(K_c(\phi-1)^2 + K_{vs}\right)\phi - ScF\phi' - 2\gamma\phi' C_6}{C_6(1+2\gamma\zeta)} \tag{35}$$

The equations mentioned above are converted into first-order ordinary differential equations by utilising the substitution of variables defined as follows:

$$\left.\begin{array}{c} F = A_1, F' = A_2, F'' = A_3, F''' = A_3' \\ \theta = A_4, \theta' = A_5, \theta'' = A_5' \\ \phi = A_6, \phi' = A_7, \phi'' = A_7' \end{array}\right\} \tag{36}$$

Equations (37)–(43) represent the necessary first-order differential equations, derived by substituting (36) into (33)–(35).

$$A_1' = A_2 \tag{37}$$

$$A_2' = A_3 \tag{38}$$

$$A_3' = \frac{C_1C_2\left(A_2^2 - A_1A_3\right) + C_1C_3\frac{M(1+H_cH_i)}{\left(H_c^2+(1+H_cH_i)^2\right)}A_2Sin^2\xi + k_pA_2 - 2\gamma A_3 - 3We\gamma(1+2\gamma\zeta)^{\frac{1}{2}}A_3^2}{(1+2\gamma\zeta) + We(1+2\gamma\zeta)^{\frac{3}{2}}A_3} \tag{39}$$

$$A_4' = A_5 \tag{40}$$

$$A_5' = \frac{-(2\gamma A_5 + \Pr Ec\frac{C_3}{C_4}\frac{M(1+H_cH_i)}{\left(H_c^2+(1+H_cH_i)^2\right)}A_2^2Sin^2\xi + \frac{1}{C_4}\Pr S_1A_4 + \frac{1}{C_4}\Pr S_2\exp(-n\zeta) + \frac{C_5}{C_4}\Pr FA_5}{(1+2\gamma\zeta)} \tag{41}$$

$$A_6' = A_7 \tag{42}$$

$$A_7' = \frac{Sc\left(K_c(A_6-1)^2 + K_{vs}\right)A_6 - ScA_1A_7 - 2\gamma A_7C_6}{C_6(1+2\gamma\zeta)} \tag{43}$$

With boundary conditions

$$\left.\begin{array}{c} A_1(0) = S_u, A_2(0) - \delta_1A_3(0) = 1, \\ A_4(0) - \delta_2A_5(0) = 1, A_7(0) = \delta_3A_6(0) \\ A_2(\infty) = 0, A_4(\infty) = 0, A_6(\infty) = 1 \end{array}\right\} \tag{44}$$

In this study, the convergence of the Runge-Kutta-Fehlberg (RKF) method, employed alongside the shooting technique, is governed by several essential criteria to ensure accuracy and stability. Primarily, the method controls the local truncation error by leveraging a fifth-order Runge-Kutta approximation and a fourth-order estimate of the error at each step. The local error must remain within a predefined tolerance, $\varepsilon_{tol} = 10^{-5}$, to ensure the solution's precision. The RKF method dynamically adjusts the step size, reducing it when the error exceeds the tolerance and increasing it when the error is significantly smaller, thus optimising computational efficiency. In this specific application, the system of boundary value problems is transformed into an initial value problem using the shooting method, necessitating the satisfaction of far-field boundary conditions. To this end, a finite value of $\zeta = 6$ and a step-size $\Delta\zeta = 10^{-5}$ are employed, ensuring the accurate approximation of asymptotic conditions at infinity. Moreover, the shooting method iteratively refines the initial guesses to match the boundary conditions at the far field, ensuring convergence. This process is repeated until the solution adheres to the initial value problem framework and the boundary conditions within an acceptable tolerance. Thus, the RKF method's adaptive step size control, coupled with the iterative shooting adjustments, ensures convergence, effectively balancing precision and computational efficiency throughout the solution process.

Table 2. Validation with Ramesh et al.[51] and Khan et al.[43]

γ	Khan et al.[43]	Ramesh et al.[51]	Present
0.1	2.10034	2.100332	2.10036
0.2	2.05886	2.058843	2.05887
0.3	2.00885	2.008887	2.00889

Results and discussions

The numerical solution for the aforementioned problem is computed using the bvp4c function in MATLAB. Table 2 presents a comparison of the velocity gradient $F''(0)$ with findings from Ramesh et al.[51] and Khan et al.,[43] under conditions where $S_u = 2.6, Pr = 0.5$, and other parameters are set to zero, which demonstrates a good computational agreement. The influences of the distinctive non-dimensional parameters $We, M, H_c, H_i, k_p, \gamma, S_u, \delta_1, \delta_2, S_1, S_2,$ and K_c on the velocity, temperature and homogeneous–heterogeneous reaction, are discussed in Figures 2 to 29. For computational purposes, the specified ranges of the varied controlling parameters are defined as:

$0.1 \leqslant \gamma \leqslant 0.8; 0.5 \leqslant M \leqslant 3; 0.1 \leqslant We \leqslant 0.4; 0.5 \leqslant k_p \leqslant 3; 0.5 \leqslant H_c \leqslant 2.5; 0.5 \leqslant H_i \leqslant 2.5; 0.1 \leqslant \delta_1 \leqslant 0.6; 0.1 \leqslant \delta_2 \leqslant 0.6; 0.1 \leqslant \delta_3 \leqslant 0.6; 0.1 \leqslant S_1 \leqslant 0.6; 0.1 \leqslant S_2 \leqslant 0.4; 0.5 \leqslant S_u \leqslant 3; 0.5 \leqslant K_c \leqslant 3; 0.5 \leqslant n \leqslant 2; 0.1 \leqslant K_{vs} \leqslant 2; 0.02 \leqslant \varphi_{Al_2O_3} \leqslant 0.1; 0.02 \leqslant \varphi_{Cu} \leqslant 0.1; \Pr = Sc = 6.5, Ec = 0.5, \xi = \frac{\pi}{4};$ based on previously considered data such as Khan et al.[43] and nanoparticles rheology.

Velocity profile

Figure 2 shows that increasing the *We*, which characterises the fluid's elastic effects and reduces the velocity profile. This happens because greater *We* increase the viscoelastic behaviour of the Williamson fluid, increasing its resistance to deformation. As a result, this higher resistance slows the fluid's travel, resulting in a lower velocity profile near the cylindrical surface. Figure 3 shows the influence of *M* on the velocity profile. A magnetic field produces a Lorentz force on the fluid, opposing its velocity. This magnetic dampening effect raises the fluid's resistive force, which reduces the velocity profile. The interaction between the magnetic field and the conductive Williamson fluid adds a further coating of drag, lowering the overall flow velocity. Figure 4 shows increasing H_c improves the velocity profile. The Hall effect, which results from the passage of charged particles in a magnetic field, alters the current distribution inside the fluid, which lowers the effective Lorentz force opposing the fluid's motion, increasing the velocity profile. Figure 5 shows that increasing the H_i results in a lower velocity profile. Ion slip describes the relative mobility of ions and neutral particles in a fluid. Higher ion slip causes higher momentum transfer between ions and fluid, increasing total drag force while decreasing the overall velocity profile. Figure 6 indicates that boosting k_p increases the medium's permeability and resistance to fluid flow, resulting in a lower velocity profile. Figure 7 shows that increasing γ leads to a higher velocity profile. This is transpiring because the curvature reduces the thickness of the boundary layer, accelerates fluid flow and polishes motion around the curved surface. Figure 8 indicates that S_u reduces the velocity profile by efficiently eliminating fluid from the boundary layer, increasing the velocity gradient at the surface and so lowering the total boundary layer velocity. Figure 9 depicts that raising δ_1 decreases the velocity profile by reducing momentum transfer from the surface to the fluid. Figures 2 to 9 consistently indicate that adding hybrid nanoparticles to the Williamson base fluid reduces the velocity profile owing to the nanofluid's higher effective viscosity and density, which increases resistance to flow and promotes interactions across the fluid framework.

Temperature Profile

Figure 2 shows that increasing the *We*, which characterises the fluid's elastic effects and reduces the velocity profile. This happens because greater *We* increase the

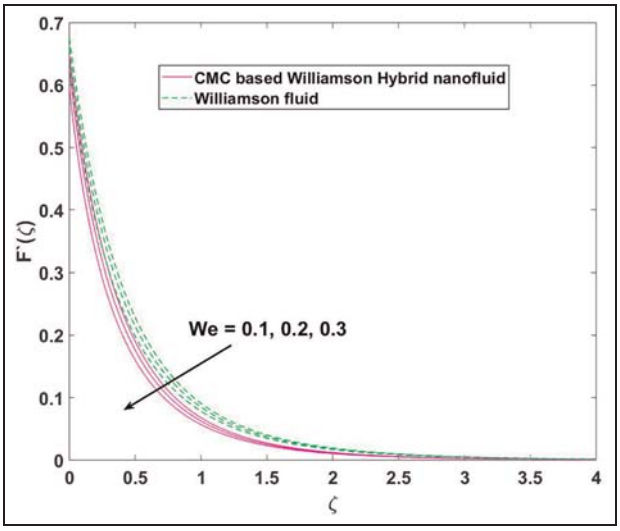

Figure 2. Impact of *We* on $F'(\zeta)$.

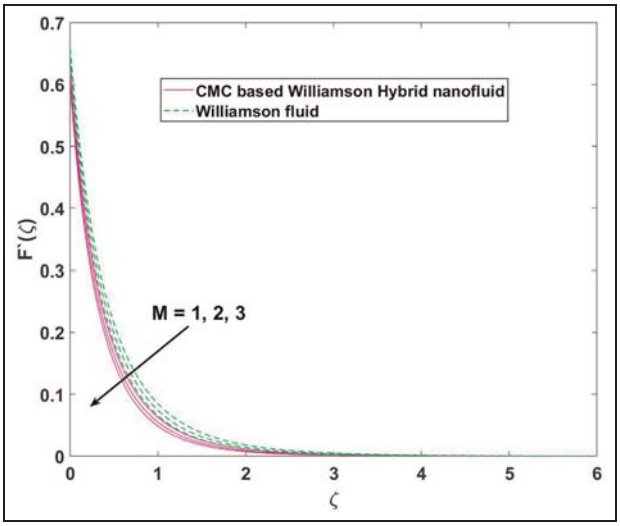

Figure 3. Impact of *M* on $F'(\zeta)$.

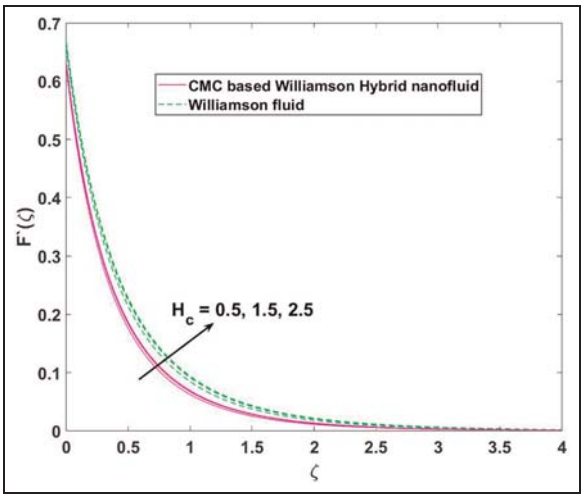

Figure 4. Impact of H_c on $F'(\zeta)$.

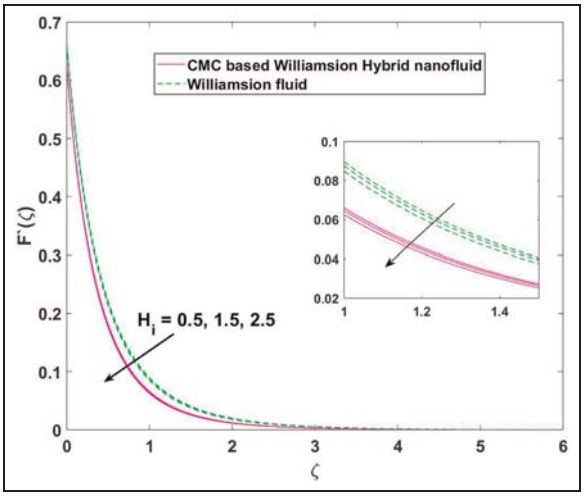

Figure 5. Impact of H_i on $F'(\zeta)$.

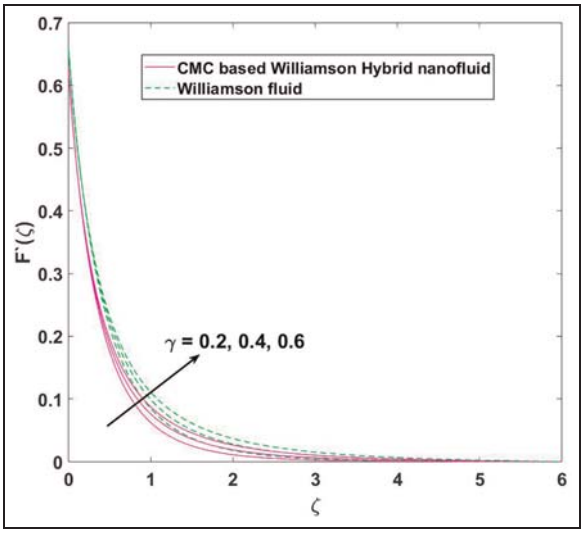

Figure 7. Impact of γ on $F'(\zeta)$.

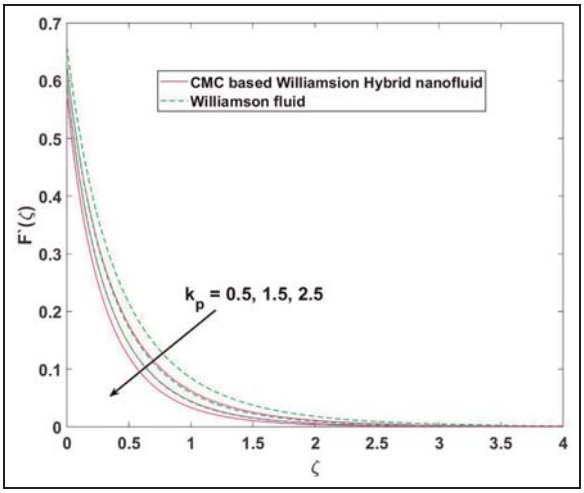

Figure 6. Impact of k_p on $F'(\zeta)$.

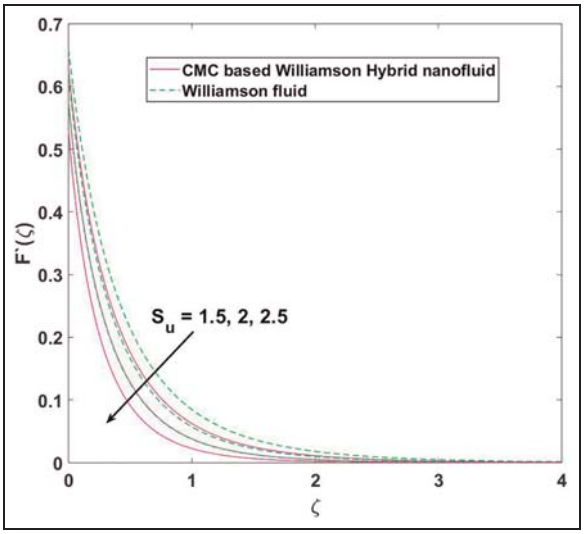

Figure 8. Impact of S_u on $F'(\zeta)$.

viscoelastic behaviour of the Williamson fluid, increasing its resistance to deformation. As a result, this higher resistance slows the fluid's travel, resulting in a lower velocity profile near the cylindrical surface. Figure 3 shows the influence of M on the velocity profile. A magnetic field produces a Lorentz force on the fluid, opposing its velocity. This magnetic dampening effect raises the fluid's resistive force, which reduces the velocity profile. The interaction between the magnetic field and the conductive Williamson fluid adds a further coating of drag, lowering the overall flow velocity. Figure 4 shows increasing H_c improves the velocity profile. The Hall effect, which results from the passage of charged particles in a magnetic field, alters the current distribution inside the fluid, which lowers the effective Lorentz force opposing the fluid's motion, increasing the velocity profile. Figure 5 shows that increasing the H_i results in a lower velocity profile. Ion slip describes the relative mobility of ions and neutral particles in a fluid. Higher ion slip causes higher momentum transfer between ions and fluid, increasing total drag force while decreasing the overall velocity profile. Figure 6 indicates that boosting k_p increases the medium's permeability and resistance to fluid flow, resulting in a lower velocity profile. Figure 7 shows that increasing γ leads to a higher velocity profile. This is transpiring because the curvature reduces the thickness of the boundary layer, accelerates fluid flow and polishes motion around the curved surface. Figure 8 indicates that S_u reduces the velocity profile by efficiently eliminating fluid from the boundary layer, increasing the velocity gradient at the surface and so lowering the total boundary layer velocity. Figure 9 depicts that raising δ_1 decreases the velocity profile by reducing momentum transfer from the surface to the fluid. Figures 2 to 9 consistently indicate that adding hybrid nanoparticles to the Williamson

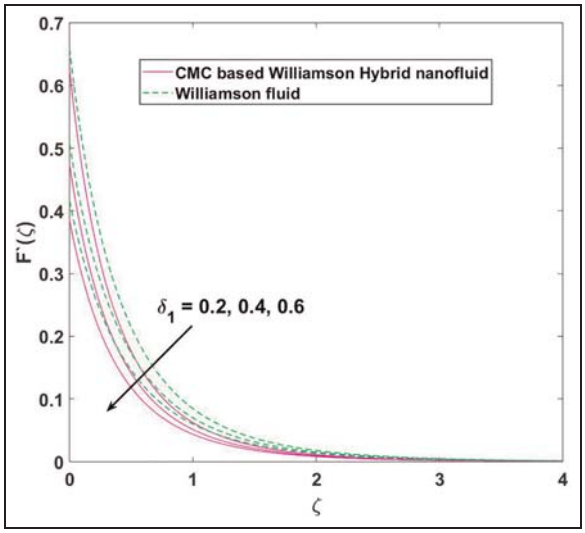

Figure 9. Impact of δ_1 on $F'(\zeta)$.

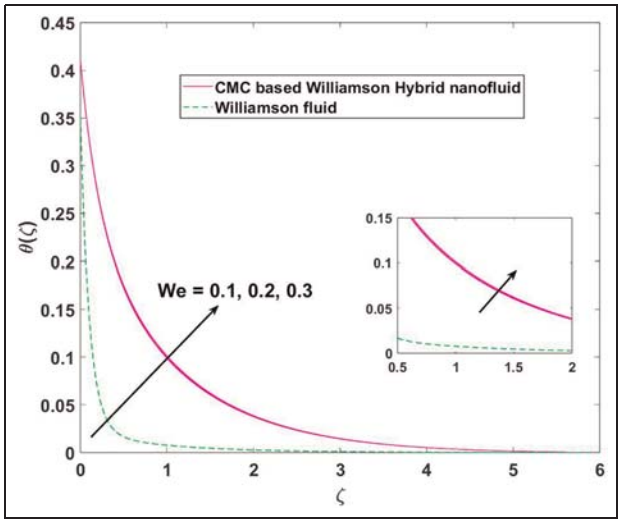

Figure 10. Impact of *We* on $\theta(\zeta)$.

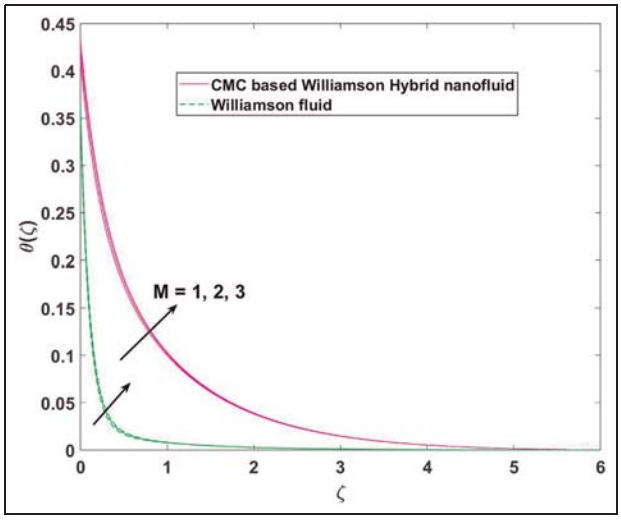

Figure 11. Impact of *M* on $\theta(\zeta)$.

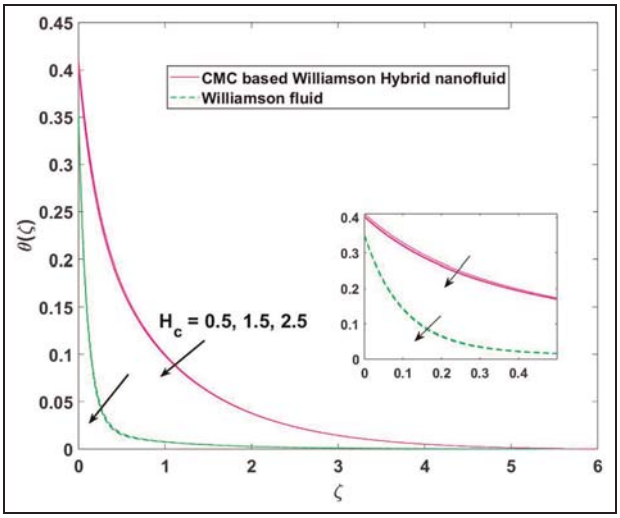

Figure 12. Impact of H_c on $\theta(\zeta)$.

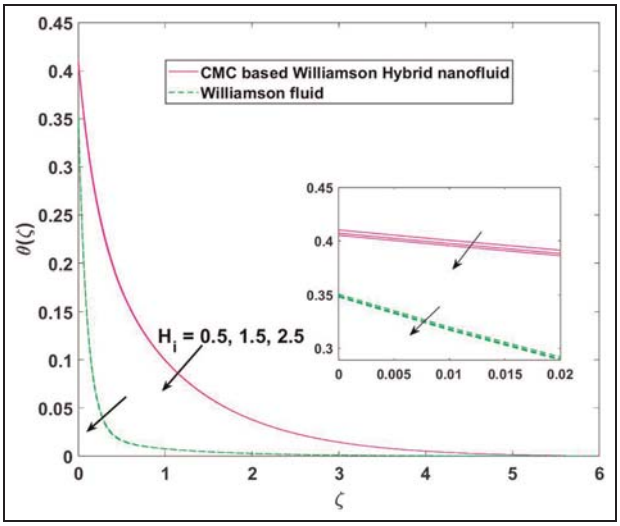

Figure 13. Impact of H_i on $\theta(\zeta)$.

base fluid reduces the velocity profile owing to the nanofluid's higher effective viscosity and density, which increases resistance to flow and promotes interactions across the fluid framework.

Homogeneous–heterogeneous reaction profile

Figure 21 illustrates that promoting *We* reduces the homogeneous-heterogeneous reaction profile due to the fluid's viscoelastic qualities, which limit molecular transport and reaction rates. Figure 22 shows *M* reduces the homogeneous-heterogeneous response profile. The magnetic field affects the fluid velocity and inhibits reactant contact, slowing the reaction rate. Figure 23 shows that H_c boosts the homogeneous-heterogeneous reaction profile by inducing extra electromagnetic forces that improve reactant mixing, resulting in faster reaction rates. Figure 24 shows that H_i raises the homogeneous-heterogeneous reaction

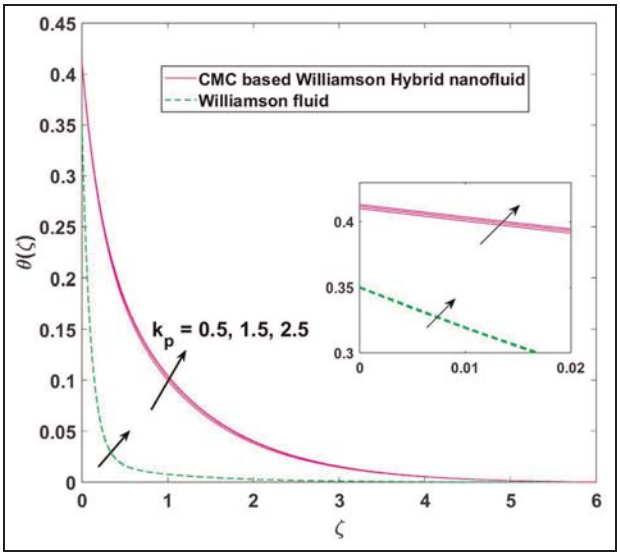

Figure 14. Impact of k_p on $\theta(\zeta)$.

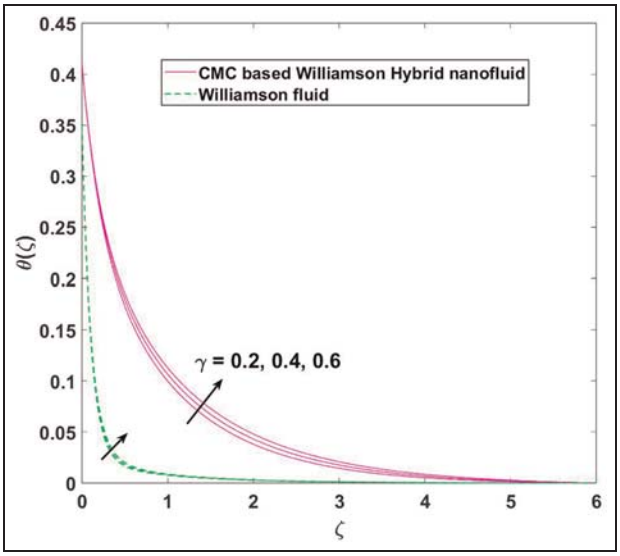

Figure 15. Impact of γ on $\theta(\zeta)$.

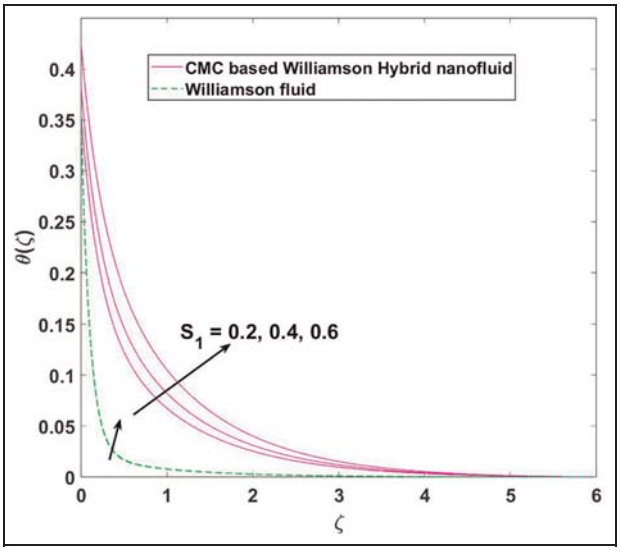

Figure 16. Impact of S_1 on $\theta(\zeta)$.

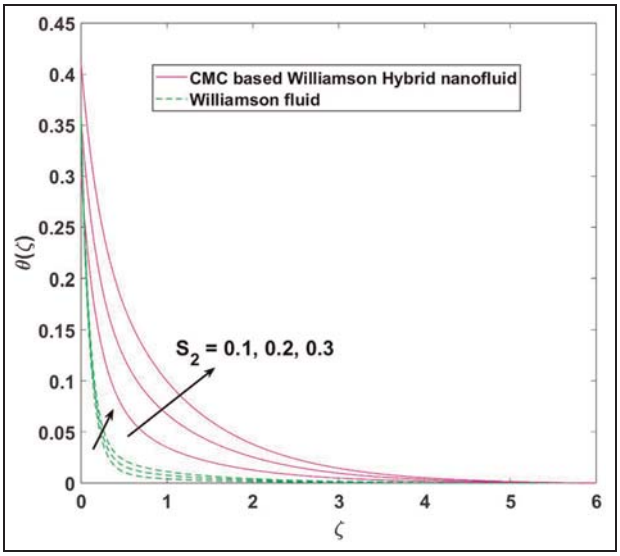

Figure 17. Impact of S_2 on $\theta(\zeta)$.

profile because it changes the fluid composition at the surface, influencing reaction kinetics and boosting reaction rates. Figure 25 illustrates how raising k_p reduces the homogeneous-heterogeneous response profile as higher porosity allows more fluid to move through the medium, which reduces the concentration of reactants available for reaction. Figure 26 shows that γ boosts the homogeneous-heterogeneous reaction profile by improving fluid mixing and increasing the surface area for reaction, resulting in greater reaction rates. Figure 27 shows that S_u boosts the homogeneous-heterogeneous reaction profile by pulling more fluid to the surface, boosting reactant availability and reaction rates. Figure 28 displays that δ_1 minimises the homogeneous-heterogeneous reaction profile by reducing momentum transfer near the surface, hence restricting reactant transport and decreasing reaction rates. Figure 29 shows that K_c reduces the homogeneous-heterogeneous reaction profile. Higher K_c values communicate stronger reaction kinetics, which leads to quicker reactant degradation and decreased overall reaction rates. Overall, in all Figures 21 to 29, adding hybrid nanoparticles to the Williamson base fluid reliably reduces the homogeneous-heterogeneous reaction profile. This decrease can be due to the nanoparticles' changed transport capabilities, viscosity effects and surface contacts, which adjust the local environment and hinder or increase reaction rates as needed.

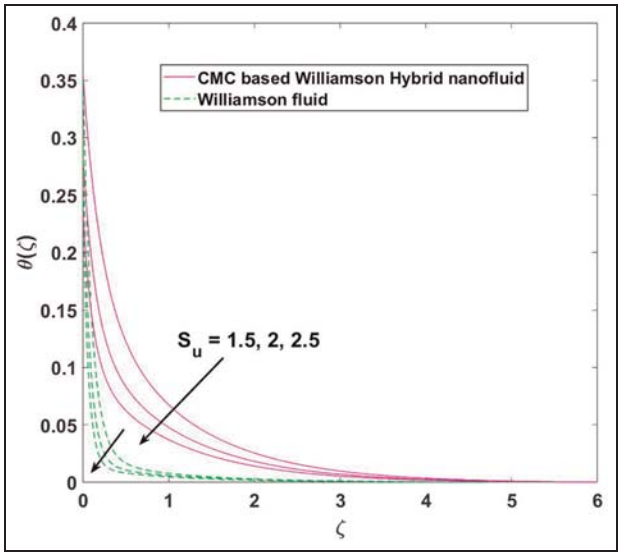

Figure 18. Impact of S_u on $\theta(\zeta)$.

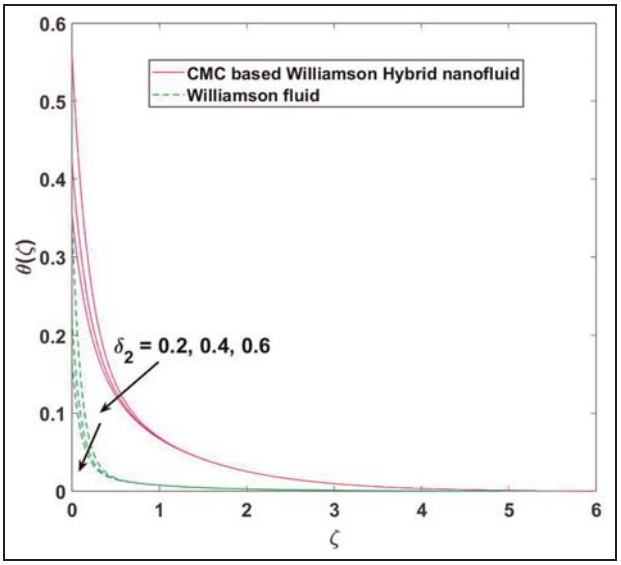

Figure 20. Impact of δ_2 on $\theta(\zeta)$.

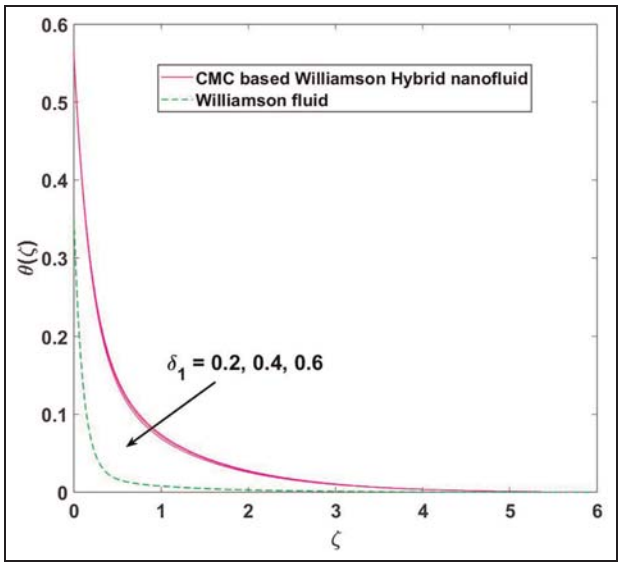

Figure 19. Impact of δ_1 on $\theta(\zeta)$.

Computational analysis of skin friction coefficient (SF) with varying hybrid nanofluid concentrations

As γ grows, the cylinder's curvature intensifies, resulting in a greater velocity gradient near the surface. This enhanced velocity gradient immediately increases tangential shear stress, which raises the SF (Table 3). Furthermore, increasing the concentration of hybrid nanoparticles increases the fluid's effective viscosity and heat conductivity. This causes a greater amount of momentum transfer at the cylinder's surface, amplifying the velocity gradient and shear stress. larger nanoparticle concentrations and a larger curvature parameter γ lead to a significant rise in SF.

The magnetic field interacts with the electric-conducting fluid, producing Lorentz forces that impede fluid velocity. This resistance raises the velocity gradient at the cylinder's surface, causing a larger shear stress and, as a result, an increased SF. Furthermore, larger nanoparticle concentrations increase the fluid's capacity to transmit momentum and heat. This increase in momentum transfer magnifies the velocity gradient at the surface in the presence of a magnetic field. As a result, when M is enhanced, the SF increases considerably with larger nanoparticle concentrations.

As We evolve, the fluid's elastic behaviour becomes more prominent, lowering the effective viscosity and hence the shear stress at the surface, resulting in a lower SK. However, increasing the concentration of hybrid nanoparticles results in a considerable increase in SK for various We values. The increased nanoparticle concentration increases the fluid's effective viscosity and thermal conductivity. The presence of additional nanoparticles accelerates momentum transfer near the surface of the cylinder, increasing the velocity gradient and the accompanying shear stress, thereby raising the skin friction coefficient. Despite a spike in SK with greater nanoparticle concentrations, the general pattern of decreased SK with increasing We are consistent across all concentrations studied. This constant pattern emphasises the fluid's viscoelastic features, as increased elastic behaviour continues to lower effective viscosity and shear stress, even as the baseline SK rises due to the presence of nanoparticles.

As k_p develops the cylinder's porous structure allowing more fluid to penetrate and interact inside the pores. This interaction causes an increase in surface area in contact with the fluid, which increases shear stress at the surface and hence the SF. Furthermore, when the concentration of hybrid nanoparticles increases, the fluid's resistance to flow rises, resulting in higher momentum transfer near the porous surface. This increased momentum transfer raises the velocity

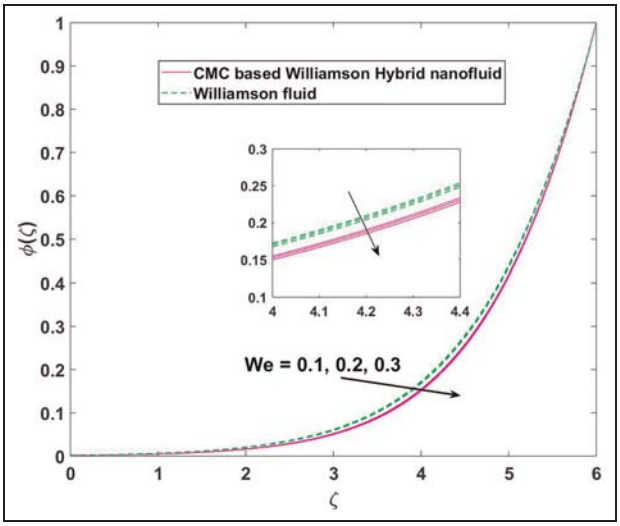

Figure 21. Impact of *We* on $\phi(\zeta)$.

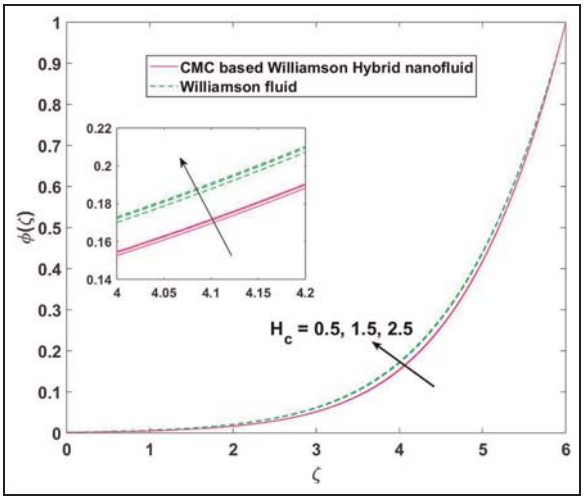

Figure 23. Impact of H_c on $\phi(\zeta)$.

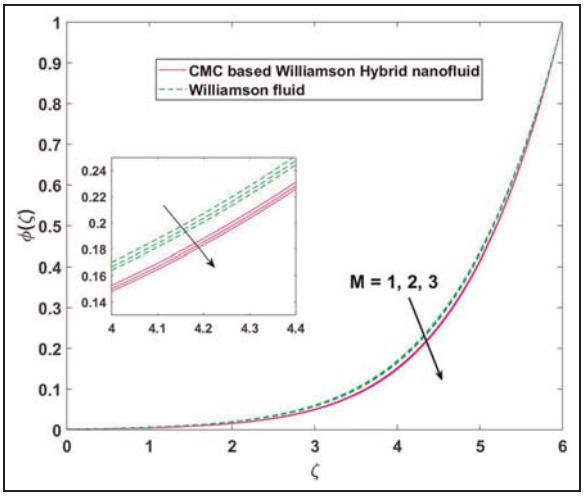

Figure 22. Impact of *M* on $\phi(\zeta)$.

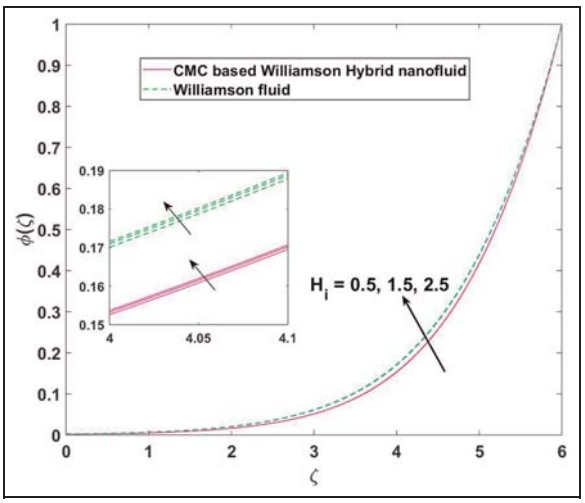

Figure 24. Impact of H_i on $\phi(\zeta)$.

gradient at the surface, resulting in more shear stress and consequently a higher SF.

As H_c improves, the secondary Hall currents offer an extra force orthogonal to both the magnetic field and the primary current, thus diminishing the Lorentz force that resists flow. This drop in Lorentz force reduces the fluid's effective viscosity, resulting in less shear stress at the surface and, as a result, a lower SF. However, when the concentration of hybrid nanoparticles grows, the SF tends to climb dramatically across different values of H_c, owing to the increasing effective viscosity and density of the nanofluid. The hybrid nanoparticles render the fluid more resistant to deformation and flow, resulting in greater momentum transfer at the cylinder's surface. This enhanced momentum transfer leads to a greater velocity gradient at the surface, elevating the shear stress and therefore raising the SF. Notwithstanding a spike in skin friction with greater nanoparticle concentrations, the general trend of decreasing skin friction with rising H_c remains consistent for all concentrations studied. This constant pattern demonstrates the dominant role of Hall currents in decreasing the Lorentz force and effective viscosity of the fluid, which continues to reduce the SF even when baseline friction is increased owing to the presence of nanoparticles.

As H_i increases, the ion slip effect reduces the effective electric force on the fluid, thereby decreasing the SF. However, increasing the concentration of hybrid nanoparticles significantly raises the skin friction coefficient for various H_i values. This rise is due to the enhanced viscosity and electrical conductivity of the nanofluid, leading to greater shear stress. Despite this, the overall trend of decreasing SF with increasing H_i persists, indicating that the ion slip effect dominates by reducing electric force and shear stress, even as nanoparticle concentration elevates the SF. Thus, the

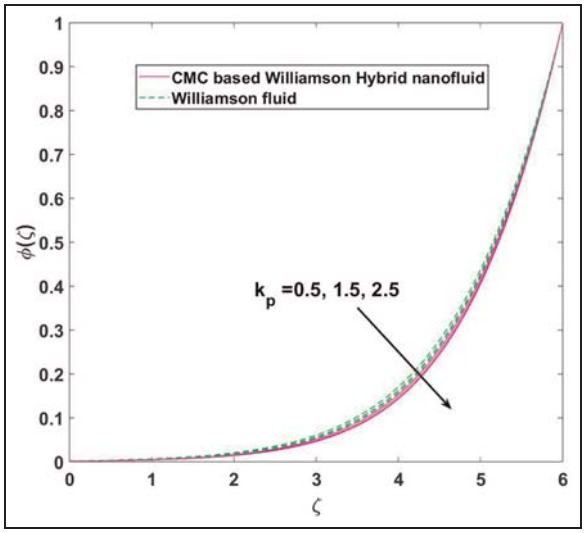

Figure 25. Impact of k_p on $\phi(\zeta)$.

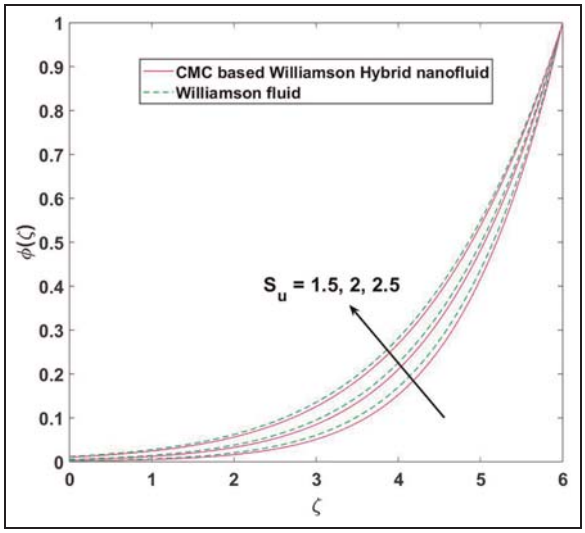

Figure 27. Impact of S_u on $\phi(\zeta)$.

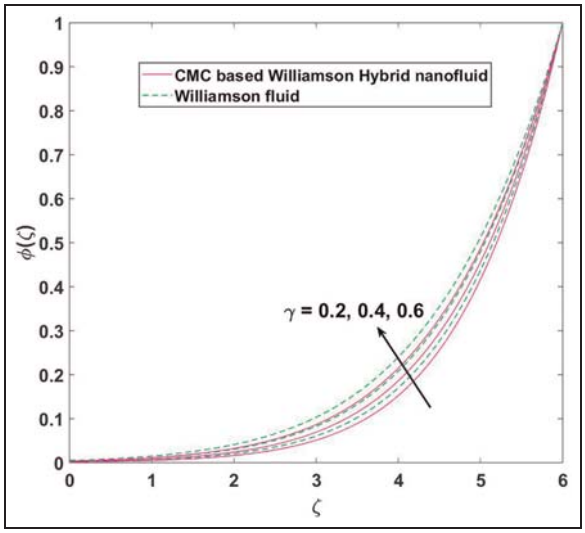

Figure 26. Impact of γ on $\phi(\zeta)$.

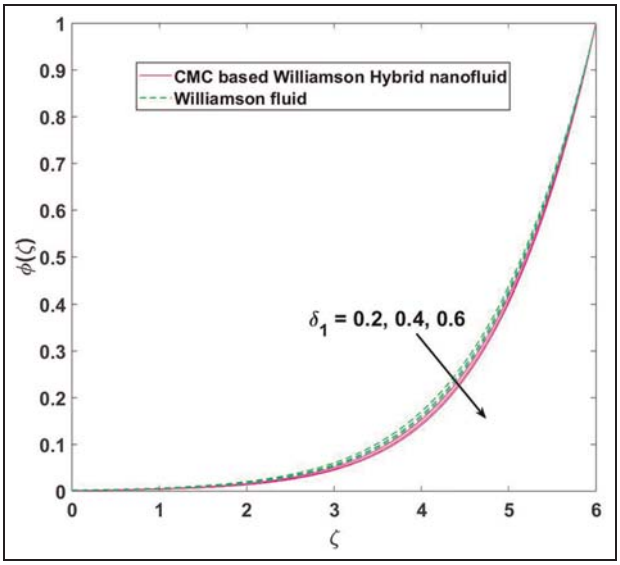

Figure 28. Impact of δ_1 on $\phi(\zeta)$.

primary impact of ion slip on lowering skin friction persists, however, increased nanoparticle concentration alters the magnitude of the SF.

At the cylinder boundary, the SF normally falls as the δ_1 increases, indicating lower momentum transfer between the fluid and the surface due to decreased relative motion. However, increasing the concentration of hybrid nanoparticles causes a significant rise in the SF throughout a range of δ_1 values. This surge is caused by increased nanofluid viscosity and density, which increase fluid resistance and momentum transfer at the boundary, raising shear stress and the SF. Regardless of the boost in nanoparticle concentration, the overall trend of decreasing SF with increasing δ_1 persists consistently across all concentrations, highlighting δ_1's dominant role in attenuating momentum transfer and shear stress, even when SF is elevated due to nanoparticle active participation.

A higher S_u increases the flow velocity near the cylinder, hence intensifying the velocity gradient at the boundary. This greater velocity gradient causes increased shear stress between the fluid and the surface, raising the SF. When the concentration of hybrid nanoparticles is raised, the SF climbs dramatically for varied S_u levels. This rise is mostly due to the nanofluid's increased effective viscosity and density as a result of the greater nanoparticle concentration. More nanoparticles in the fluid increase its resistance to flow, resulting in greater momentum transfer at the surface. As a result, the velocity gradient and related shear stress are amplified, increasing the SF even more.

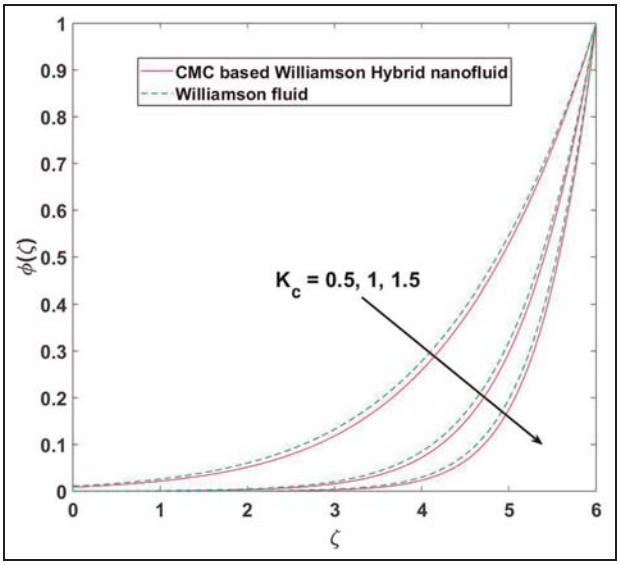

Figure 29. Impact of K_c on $\phi(\zeta)$.

The SF exhibits no variation with increases in $\delta_2, \delta_3, S_1, S_2,$ and K_c. This constancy arises because these parameters might primarily influence the thermal and chemical characteristics of the fluid, without directly impacting the fluid's momentum transfer and shear stress near the surface of the cylinder. However, as the concentration of hybrid nanoparticles develops the SF rises dramatically across all of these parameters, owing to the increased effective viscosity and density of the nanofluid caused by the greater nanoparticle concentration. As nanoparticle concentration increases, the fluid's resistance to flow increases, resulting in higher momentum transfer near the cylinder surface. This increased momentum transfer raises the velocity gradient and shear stress, raising the SF. This computational research contributes to understanding the critical significance of nanoparticle concentration in SF, even though other parameters are inert in this respect.

Table 3. Effect of different parameters on skin friction coefficient (SF) with varying hybrid nanoparticle concentrations.

Parameters ↓	Hybrid nanoparticle concentrations $(\varphi_{Al_2O_3} + \varphi_{Cu}) \rightarrow$				
	4%	8%	12%	16%	20%
γ (0.2,0.4,0.6)	−1.26515	−1.42650	−1.60012	−1.78851	−1.99435
	−1.27873	−1.44038	−1.61482	−1.80457	−2.01237
	−1.29229	−1.45437	−1.62970	−1.82086	−2.03065
M (0.6,0.8,1.0)	−1.24642	−1.40647	−1.57830	−1.76436	−1.96727
	−1.25594	−1.41665	−1.58938	−1.77663	−1.98103
	−1.26515	−1.42650	−1.60012	−1.78851	−1.99435
We (0.1,0.2,0.3)	−1.32204	−1.49221	−1.67487	−1.87253	−2.08791
	−1.26515	−1.42650	−1.60012	−1.78851	−1.99435
	−1.20222	−1.35355	−1.51697	−1.69498	−1.89022
k_p (0.5,1.0,1.5)	−1.26515	−1.42650	−1.60012	−1.78851	−1.99435
	−1.32327	−1.48802	−1.66664	−1.86179	−2.07635
	−1.37147	−1.53929	−1.72224	−1.92310	−2.14495
H_c (0.5,1.0,1.5)	−1.26515	−1.42650	−1.60012	−1.78851	−1.99435
	−1.24975	−1.41004	−1.58218	−1.76866	−1.97208
	−1.24043	−1.40008	−1.57134	−1.75665	−1.95862
H_i (0.5,1.0,1.5)	−1.26515	−1.42650	−1.60012	−1.78851	−1.99435
	−1.25920	−1.42013	−1.59318	−1.78083	−1.98574
	−1.25434	−1.41495	−1.58753	−1.77458	−1.97872
δ_1 (0.2,0.4,0.6)	−1.45371	−1.64313	−1.84568	−2.06411	−2.30133
	−1.12329	−1.26426	−1.41668	−1.58284	−1.76520
	−0.92165	−1.03467	−1.15774	−1.29280	−1.44196
δ_2 (0.2,0.4,0.6)	−1.26515	−1.42650	−1.60012	−1.78851	−1.99435
	−1.26515	−1.42650	−1.60012	−1.78851	−1.99435
	−1.26515	−1.42650	−1.60012	−1.78851	−1.99435
δ_3 (0.2,0.4,0.6)	−1.26515	−1.42650	−1.60012	−1.78851	−1.99435
	−1.26515	−1.42650	−1.60012	−1.78851	−1.99435
	−1.26515	−1.42650	−1.60012	−1.78851	−1.99435
S_1 (0.2,0.4,0.6)	−1.26515	−1.42650	−1.60012	−1.78851	−1.99435
	−1.26515	−1.42650	−1.60012	−1.78851	−1.99435
	−1.26515	−1.42650	−1.60012	−1.78851	−1.99435
S_2 (0.2,0.3,0.4)	−1.26515	−1.42650	−1.60012	−1.78851	−1.99435
	−1.26515	−1.42650	−1.60012	−1.78851	−1.99435
	−1.26515	−1.42650	−1.60012	−1.78851	−1.99435
S_u (0.8,1.0,1.2)	−1.21173	−1.36466	−1.52978	−1.70949	−1.90640
	−1.26515	−1.42650	−1.60012	−1.78851	−1.99435
	−1.31773	−1.48718	−1.66900	−1.86584	−2.08044
K_c (0.2,0.4,0.6)	−1.26515	−1.42650	−1.60012	−1.78851	−1.99435
	−1.26515	−1.42650	−1.60012	−1.78851	−1.99435
	−1.26515	−1.42650	−1.60012	−1.78851	−1.99435

Computational analysis of local Nusselt number (Nu) with varying hybrid nanofluid concentrations

As various parameters evolve, the Nu generally shows a decreasing trend due to their respective impacts on the fluid dynamics and thermal boundary layer characteristics. The increased γ, M, We, k_p all contribute to thickening the thermal boundary layer, thereby reducing the temperature gradient at the surface and lowering the convective heat transfer rate. This trend remains consistent across different concentrations of hybrid nanoparticles.

However, as the concentration of hybrid nanoparticles increases, the Nu rises significantly across a range of these parameters due to increased thermal conductivity and viscosity of the nanofluid, which improves heat transfer efficiency. Higher thermal conductivity enables more efficient heat conduction, whereas increased viscosity improves momentum and thermal interactions within the boundary layer, resulting in faster convective heat transfer rates.

For γ, despite the induced larger thermal boundary layer reducing the temperature differential and convective heat transfer, the presence of hybrid nanoparticles modifies the fluid's thermal properties, significantly elevating the convective heat transfer rate. With increasing M, the damping effect reduces fluid motion and thickens the thermal boundary layer but still the improved thermal characteristics of the nanofluid due to higher nanoparticle concentration significantly increase the Nu, enhancing the overall heat transfer efficiency. In the case of We in Williamson fluid, the viscoelastic properties inhibit fluid motion, creating a thicker thermal boundary layer and lowering the convective heat transfer rate. However, the superior heat conduction and improved thermal energy distribution due to higher nanoparticle concentration significantly raise the Nu, altering the heat transfer efficiency. Lastly, for k_p, the enhanced permeability of the porous medium reduces fluid velocity and thickens the thermal boundary layer. Despite this, the higher thermal conductivity and improved viscosity of the nanofluid lead to a notable increase in the Nu, enhancing the convective heat transfer rate across various values of k_p.

As the electromagnetic effects improve thermal mixing and enhance fluid motion, the Nu for the cylinder increases as the H_c and H_i rise. By causing secondary flows that are perpendicular to the primary flow direction, the Hall current improves convective heat transfer. Similar to this, the ion slip parameter affects the surface of the cylinder's electric double layer, which results in enhanced electrokinetic effects that promote more effective thermal energy transfer. The Nu for both H_c and H_i increases noticeably with increasing hybrid nanoparticle concentration. This increase is explained by the nanofluid's increased viscosity and thermal conductivity, both of which improve the heat transfer efficiency. While the elevated viscosity encourages more efficient thermal energy distribution within the fluid, the increased thermal conductivity permits more efficient heat conduction. As a result, the enhanced convective heat transfer rate and consequently higher Nu are produced by the synergistic effects of higher H_c and H_i in conjunction with the nanofluid's superior thermal properties.

At the cylinder's boundary, the Nu decreases as the values of δ_1 and δ_2 increase. This is because δ_2 lowers the heat exchange efficiency between the fluid and the surface, creating a thicker thermal boundary layer and a lower temperature gradient, while δ_1 weakens convective heat transfer by reducing the fluid's adherence to the surface. Notwithstanding, for all values of δ_1 and δ_2, the Nu increases significantly as the concentration of hybrid nanoparticles increases. The increased viscosity and thermal conductivity of the nanofluid are the cause of this notable increase. Better heat conduction is made possible by the increased thermal conductivity, and better thermal energy distribution within the fluid is encouraged by the increased viscosity. The enhanced thermal properties of the nanofluid due to the higher concentration of hybrid nanoparticles significantly elevate the Nu, enhancing the convective heat transfer efficiency across all considered concentrations, despite the overall trend of decreasing Nu with increasing δ_1 and δ_2. Thus, while δ_1 and δ_2 inherently reduce heat transfer efficiency, the superior thermal characteristics of the nanofluid counteract this effect, leading to a significant rise in the Nu.

For the cylinder, higher values of S_1 and S_2 increase internal heat generation within the fluid, resulting in a thicker thermal boundary layer and a reduced temperature gradient at the surface, which diminishes the convective heat transfer rate. As a result, the Nu decreases with an increase in both of these parameters. Yet, as the concentration of hybrid nanoparticles increases, the Nu climbs dramatically across various values of S_1 and S_2 due to the nanofluid's increased thermal conductivity and viscosity, which improves heat transfer efficiency. Despite the general tendency of decreasing Nu with rising S_1 and S_2 across all concentrations, the addition of hybrid nanoparticles dramatically increases the Nu. This elevation illustrates that, while heat source characteristics naturally expand the thermal boundary layer and lessen the temperature gradient, the increased thermal properties of the nanofluid owing to increasing nanoparticle concentrations significantly alter heat transfer efficiency.

Although the Nu normally rises with the S_u, for S_u values less than 0.8, Nu tends to fall as the concentration of hybrid nanoparticles increases. This drop in lower S_u values can be linked to an intensified thermal boundary layer caused by inadequate suction, which prevents effective convective heat transfer despite the nanofluid's increased thermal conductivity and viscosity. The hybrid nanoparticles increase thermal characteristics, however, the restricted suction cannot adequately counteract boundary layer thickening, leading to a reduced temperature gradient and decreased

Nu. In contrast, for higher S_u values, the Nu increases drastically as the nanoparticle concentration rises. In this regime, increased suction effectively thins the thermal boundary layer, resulting in a larger temperature gradient at the surface and improved convective heat transfer. The nanofluid's enhanced heat conductivity and viscosity amplify this effect, resulting in a significant increase in Nu. As a result, a relationship between the S_u and the hybrid nanoparticle concentration has a considerable impact on the convective heat transfer rate, with higher S_u values taking advantage of the nanofluid's better thermal characteristics to produce higher heat transfer efficiency.

Variations in the δ_3 and K_c do not affect the Nu because these reaction parameters mainly affect the chemical kinetics and not the thermal boundary layer properties or the convective heat transfer mechanism directly. However, for all values of these parameters, the Nu increases significantly with increasing hybrid nanoparticle concentration. Consequently, the presence of hybrid nanoparticles significantly increases the Nu by enhancing the fluid's capacity to conduct and distribute heat, even though δ_3 and K_c have no direct effect on the convective heat transfer rate.

Computational quantification of hybrid nanoparticle concentration on skin friction and thermal transfer in CMC-based Williamson hybrid nanofluid

The purpose of this investigation is to determine how the concentration of hybrid nanoparticles affects the skin friction coefficient and local Nusselt number of a CMC-based Williamson hybrid nanofluid. The percentage changes in these two characteristics are determined by comparing the Williamson base fluid to various concentrations of hybrid nanoparticles (4%, 8%, 12%, 16% and 20%). To begin, we compute the skin friction coefficient (SF_{base}) and local Nusselt number (Nu_{base}) for the Williamson fluid in the absence of nanoparticles, followed by the skin friction coefficient (SF_c) and local Nusselt number (Nu_c) for hybrid nanofluids at concentrations c.

To compute the percentage change in skin friction coefficient for each concentration c of hybrid nanoparticles, we use the formula below:

$$\%\Delta SF_c = \left(\frac{SF_c - SF_{base}}{SF_{base}}\right)\times 100\% \tag{45}$$

where, SF_{base} is the skin friction coefficient of the base Williamson fluid and SF_c is the skin friction coefficient of the hybrid nanofluid at concentration c.

Similarly, the percentage change in the local Nusselt number for each concentration c of hybrid nanoparticles is calculated using the formula:

$$\%\Delta Nu_c = \left(\frac{Nu_c - Nu_{base}}{Nu_{base}}\right)\times 100\% \tag{46}$$

where, Nu_{base} is the local Nusselt number of the base Williamson fluid and Nu_c is the local Nusselt number of the hybrid nanofluid at concentration c.

The computed values using (45), and (46) are tabulated in Table 4.

Table 5 highlights a dramatic rise in the skin friction coefficient for Williamson hybrid nanofluids compared to the base Williamson fluid. This increase becomes more pronounced with higher nanoparticle concentrations. This surge is primarily driven by the significant increase in viscosity, which enhances resistance to fluid flow and amplifies shear stress at the boundary layer. Furthermore, the nanoparticles boost effective momentum transfer within the fluid, intensifying frictional forces at the surface.

Again, in this investigation, we observed that adding hybrid nanoparticles into a CMC-based Williamson nanofluid resulted in a negative percentage change in the Nusselt number at 4% concentration. In contrast, there were positive improvements ranging from 8% to 20%. This early decrease can be ascribed to poor dispersion, nanoparticle agglomeration, increased viscosity and insufficient particle-fluid interactions at lower concentrations. As the nanoparticle concentration increases, these issues are alleviated, resulting in improved thermal conductivity and convective heat transfer, yielding positive changes in the Nusselt number, emphasising the critical importance of optimising nanoparticle concentration to effectively improve the thermal performance of nanofluids.

Furthermore, in the investigation of CMC-based Williamson hybrid nanofluids, it was shown that increasing nanoparticle concentration resulted in a greater increase in the skin friction coefficient than the Nusselt number. This can be associated with a significant rise in viscosity, which increases shear stress and boundary layer thickness, resulting in greater skin friction. Furthermore, particle-fluid interactions enhance momentum transfer, resulting in greater frictional forces. In contrast, an increase in thermal conductivity does not proportionately increase the Nusselt number because of the concomitant rise in viscosity and probable fall in the Reynolds number, which restricts convective heat transfer efficiency.

Conclusion

The current investigation explored the flow of CMC-based Williamson hybrid nanofluid over a porous, horizontally stretched cylindrical geometry, particularly under the combined effects of Hall current, ion slip, a diagonal magnetic field ($\xi = 45°$), suction, velocity slip

Table 4. Effect of different parameters on local Nusselt number (Nu) with varying hybrid nanoparticle concentrations.

Parameters ↓	Hybrid nanoparticle concentrations $(\varphi_{Al_2O_3} + \varphi_{Cu}) \rightarrow$				
	4%	8%	12%	16%	20%
γ (0.2,0.4,0.6)	1.59620	1.65403	1.69787	1.72313	1.72390
	1.55930	1.59702	1.61180	1.59610	1.54123
	1.51746	1.53404	1.52052	1.47033	1.38002
M (0.6,0.8,1.0)	1.62498	1.68767	1.73801	1.77195	1.78435
	1.61028	1.67050	1.71753	1.74707	1.75355
	1.59620	1.65403	1.69787	1.72313	1.72390
We (0.1,0.2,0.3)	1.60591	1.66640	1.71346	1.74274	1.74868
	1.59620	1.65403	1.69787	1.72313	1.72390
	1.58460	1.63920	1.67909	1.69941	1.69380
k_p (0.5,1.0,1.5)	1.59620	1.65403	1.69787	1.72313	1.72390
	1.56697	1.61915	1.65516	1.66937	1.65422
	1.54103	1.58802	1.61673	1.62048	1.58993
H_c (0.5,1.0,1.5)	1.59620	1.65403	1.69787	1.72313	1.72390
	1.61982	1.68164	1.73082	1.76322	1.77356
	1.63429	1.69854	1.75096	1.78767	1.80379
H_i (0.5,1.0,1.5)	1.59620	1.65403	1.69787	1.72313	1.72390
	1.60529	1.66466	1.71056	1.73858	1.74305
	1.61273	1.67337	1.72095	1.75122	1.75870
δ_1 (0.2,0.4,0.6)	1.62439	1.68847	1.74003	1.77509	1.78862
	1.57058	1.62264	1.65919	1.67498	1.66306
	1.52567	1.56744	1.59060	1.58844	1.55160
δ_2 (0.2,0.4,0.6)	2.02041	2.06661	2.09374	2.09700	2.07017
	1.31922	1.37878	1.42789	1.46240	1.47686
	0.97933	1.03447	1.08336	1.12266	1.14788
δ_3 (0.2,0.4,0.6)	1.59620	1.65403	1.69787	1.72313	1.72390
	1.59620	1.65403	1.69787	1.72313	1.72390
	1.59620	1.65403	1.69787	1.72313	1.72390
S_1 (0.2,0.4,0.6)	1.88030	1.99892	2.11525	2.22809	2.33620
	1.71427	1.79982	1.87762	1.94525	1.99986
	1.43755	1.45089	1.43601	1.38079	1.26625
S_2 (0.2,0.4,0.6)	1.59620	1.65403	1.69787	1.72313	1.72390
	1.23900	1.25215	1.24814	1.22177	1.16630
	0.88180	0.85027	0.79842	0.72040	0.60871
S_u (0.8,1.0,1.2)	1.18148	1.15787	1.10119	0.99772	0.82644
	1.59620	1.65403	1.69787	1.72313	1.72390
	1.88445	1.99169	2.09203	2.18266	2.26024
K_c (0.2,0.4,0.6)	1.59620	1.65403	1.69787	1.72313	1.72390
	1.59620	1.65403	1.69787	1.72313	1.72390
	1.59620	1.65403	1.69787	1.72313	1.72390

and thermal slip. This study is unique in its use of both uniform and exponential space-dependent heat sources. Additionally, it analyses the influence of homogeneous-heterogeneous reactions and employs the Runge-Kutta-Fehlberg method to examine the skin friction and local Nusselt number across various nanoparticle concentrations, providing a comparative graphical analysis between CMC-based Williamson hybrid nanofluid and Williamson fluid. The Runge-Kutta-Fehlberg method is used for computation and the Hamilton-Crosser model for thermophysical correlation is used. The major interpretations from this investigation are:

1. The study finds that $We, M,$ and k_p reduce both the velocity and homogeneous-heterogeneous reaction profiles while enhancing the thermal profile. Similarly, incorporating hybrid nanoparticles into CMC-Williamson fluids lowers the velocity and reaction profiles but boosts the thermal profile.
2. H_c increases both the velocity and reaction profiles while decreasing the thermal profile. Conversely, H_i reduces the velocity and thermal profiles but increases the reaction profile.
3. The thermal profile rises sharply with the addition of hybrid nanoparticles for S_1, though this change is minimal in CMC-based Williamson fluids. S_2, however, equally enhances the thermal profile for both CMC-based Williamson hybrid nanofluid and Williamson fluid.
4. S_u decreases both the velocity and thermal profiles but elevates the homogeneous-heterogeneous reaction profile. The presence of hybrid nanoparticles amplifies changes in the velocity and thermal profiles, though the reaction profile shows less variation.

Table 5. Change in skin friction coefficient and local Nusselt number with varying hybrid nanoparticle concentrations for CMC-based Williamson hybrid nanofluid in comparison with Williamson fluid.

Skin friction coefficient of Williamson fluid	Local Nusselt number of Williamson fluid	Concentration of hybrid nanoparticles (%)	Skin friction coefficient of Williamson hybrid nanofluid	% Change in skin friction coefficient	Local Nusselt number of Williamson hybrid nanofluid	% Change in local Nusselt number
At 0% concentration of nanoparticles		In the presence of nanoparticles with varying concentration from 4% to 20%				
−1.41620	3.24702	4%	−1.62147	14.49%	3.05789	−5.82%
		8%	−1.83684	29.70%	3.26117	0.43%
		12%	−2.06561	45.85%	3.46208	6.21%
		16%	−2.31100	63.18%	3.65908	12.69%
		20%	−2.57621	81.91%	3.85056	18.58%

5. Velocity slip decreases all profiles, while thermal slip significantly diminishes the thermal profile.
6. Increasing the concentration of hybrid nanoparticles consistently amplifies SF across various parameters. Despite variations in parameters such as γ, M and k_p, the dominant trend is a significant rise in SF with higher nanoparticle concentrations.
7. While factors like We, H_c, and H_i effects generally reduce shear stress and SF, the presence of nanoparticles counteracts these trends by boosting effective viscosity and momentum transfer.
8. Increasing the concentration of hybrid nanoparticles markedly enhances Nu across various parameters which leads to more efficient heat transfer, even in scenarios where thicken the thermal boundary layer and reduce convective heat transfer.
9. At lower S_u values, the Nu decreases with increasing nanoparticles but at higher S_u values lead to a larger temperature gradient and a substantial increase in Nu.
10. Following enhanced viscosity, raising the concentration of hybrid nanoparticles improves SF in CMC-based Williamson nanofluids, hence boosting shear stress and momentum transfer. While heat conductivity improves, viscosity increases, limiting the Nu's development. Effective suction improves thermal performance by reducing the thermal boundary layer and increasing heat transfer efficiency.

Practical implementation and future direction

The present findings have practical implications across various applications involving flow across a cylinder, especially when considering factors like Hall current, ion slip, magnetic field, porosity, heat source and homogeneous-heterogeneous reactions, along with boundary conditions such as velocity slip, thermal slip and suction, which include:

- CMC-based Williamson hybrid nanofluids can optimise thermal management in magnetic fields and porous media, resulting in more efficient magnetic drug targeting devices and porous heat exchangers.
- Using CMC-based Williamson hybrid nanofluids in MHD systems improves fluid flow control and efficiency in generators and pumps by leveraging Hall current and ion slip effects.
- Optimising thermal management in reactors and chemical processing equipment through the use of nanofluids and heat source effects. This method improves efficiency by accurately managing temperature distribution while minimising energy use.
- Using nanofluids with velocity slip, thermal slip and suction boundary conditions improves flow

control and thermal insulation and reduces drag in microfluidic and nanofluidic systems, leading to better overall performance.
- Featuring CMC-based Williamson hybrid nanofluids in electronic cooling systems improves thermal conductivity and convective heat transfer, improving component reliability and stability.

For future research, the authors recommend investigatinge dynamics using alternative base fluids, such as Sodium Alginate, which exhibits characteristics similar to Williamson fluid and nanoparticles possessing distinctive properties. Additionally, varying the particle concentration may yield further insights, particularly in ternary and quaternary nanofluids. It is also advisable to extend the current study to different geometrical configurations, incorporating practical applications and appropriate boundary conditions to enhance the applicability of the findings.

Acknowledgements

Not applicable

Author Note

Neelav Sarma is also affiliated with the Department of Mathematics at The Assam Royal Global University in Guwahati, Assam, India.

Declaration of conflicting interests

The author(s) declared no potential conflicts of interest with respect to the research, authorship, and/or publication of this article.

Funding

The author(s) received no financial support for the research, authorship, and/or publication of this article.

Ethics approval and consent to participate

Not applicable

Consent for publication

Not applicable

ORCID iD

Neelav Sarma https://orcid.org/0000-0002-4445-3621

Availability of data and materials

Data has been included within the manuscript, wherever applicable.

References

1. Williamson RV. The flow of pseudoplastic materials. *Ind Eng Chem* 1929; 21(11): 1108–1111.
2. Nadeem S and Akram S. Peristaltic flow of a Williamson fluid in an asymmetric channel. *Commun Nonlinear Sci Numer Simul* 2010; 15(7): 1705–1716.
3. Iqbal W, Naeem MN and Jalil M. Numerical analysis of Williamson fluid flow along an exponentially stretching cylinder. *AIP Adv* 2019; 9(5): 055118. DOI: 10.1063/1.5092737
4. Rashid M, Ansar K and Nadeem S. Effects of induced magnetic field for peristaltic flow of Williamson fluid in a curved channel. *Physica A* 2020; 553: 123979.
5. Loganathan P and Dhivya M. Heat and mass transfer analysis of a convective Williamson fluid flow over a cylinder. *Int J Fluid Mech Res* 2020; 47(2): 171–189.
6. Shah Z, Raja MAZ and Shoaib M. Design of Bayesian stochastic networks for numerical treatment of Williamson fluid stretching flow model with mixed convected heat generation. *Numer Heat Transf B Fundam* 2024; 1–24. DOI: 10.1080/10407790.2024.2329253
7. Sharma KR and Jain S. An unsteady MHD Williamson fluid flow in a vertical porous channel with porous media and thermal radiation. *Int J Adv Eng Sci Appl Math* 2024; 16(3): 274–285.
8. Gangadhar K, Sangeetha Rani M and Wakif A. Non-Fourier heat flux and joule dissipation in hybrid nanoparticles suspension with Williamson fluid. *Eur Phys J Plus* 2024; 139(4): 1–11.
9. Zaman SU, Aslam MN, Riaz MB, et al. Williamson MHD nanofluid flow with radiation effects through slender cylinder. *Results Eng* 2024; 22: 101966.
10. Akbar NS, Maraj EN, Shah SI, et al. Nano particle distribution in blood via electroosmotic peristaltic flow in a non-uniform wavy membrane base capillaries. *Sens Actuators A Phys* 2024; 376: 115626.
11. Kulkarni M and Shankar HF. Numerical investigation of mixed convective Williamson nanofluid flow over a stretching/shrinking wedge in the presence of chemical reaction parameter and liquid hydrogen diffusion. *Numer Heat Transf A Appl* 2024; 1–14. DOI: 10.1080/10407782.2024.2335550
12. Akram J and Akbar NS. Electroosmotically actuated peristaltic-ciliary flow of propylene glycol + water conveying titania nanoparticles. *Sci Rep* 2023; 13(1): 11801.
13. Ghadikolaei SS, Hosseinzadeh K and Ganji DD. Numerical study on magnetohydrodynic CNTs-water nanofluids as a micropolar dusty fluid influenced by non-linear thermal radiation and joule heating effect. *Powder Technol* 2018; 340: 389–399.
14. Turcu R, Darabont A, Nan A, et al. New polypyrrole-multiwall carbon nanotubes hybrid materials. *J Optoelectron Adv Mater* 2006; 8(2): 643–647.
15. Ranga Babu JA, Kumar KK and Srinivasa Rao S. State-of-art review on hybrid nanofluids. *Renew Sustain Energ Rev* 2017; 77: 551–565.
16. Suresh S, Venkitaraj KP, Selvakumar P, et al. Synthesis of Al2O3–Cu/water hybrid nanofluids using two step method and its thermo physical properties. *Colloids Surf A Physicochem Eng Asp* 2011; 388(1-3): 41–48.
17. Zainal NA, Nazar R, Naganthran K, et al. Slip effects on unsteady mixed convection of hybrid nanofluid flow near the stagnation point. *Appl Math Mech* 2022; 43(4): 547–556.
18. Ghadikolaei SS, Yassari M, Sadeghi H, et al. Investigation on thermophysical properties of TiO2-Cu/H2O hybrid nanofluid transport dependent on shape factor in

MHD stagnation point flow. *Powder Technol* 2017; 322: 428–438.
19. Adnan Abbas W, Bani-Fwaz ZM, et al. Thermal efficiency of radiated tetra-hybrid nanofluid [(Al_2O_3-CuO-TiO_2-Ag)/water]$_{tetra}$ under permeability effects over vertically aligned cylinder subject to magnetic field and combined convection. *Sci Prog* 2023; 106(1): 00368504 221149797.
20. Zubair T, Usman M, Hamid M, et al. Computational analysis of radiative Williamson hybrid nanofluid comprising variable thermal conductivity. *Jpn J Appl Phys* 2021; 60(8): 087004.
21. Akbar NS, Rafiq M, Muhammad T, et al. Electro osmotically interactive biological study of thermally stratified micropolar nanofluid flow for copper and silver nanoparticles in a microchannel. *Sci Rep* 2024; 14(1): 518.
22. Ghadikolaei SS, Hosseinzadeh K and Ganji DD. Investigation on ethylene glycol-water mixture fluid suspend by hybrid nanoparticles (TiO_2-CuO) over rotating cone with considering nanoparticles shape factor. *J Mol Liq* 2018; 272: 226–236.
23. Paul A, Sarma N and Patgiri B. Numerical Assessment of MHD thermo-mass flow of Casson ternary hybrid nanofluid around an exponentially stretching cylinder. *BioNanoScience* 2024; 14(5): 5230–5245.
24. Guo P, Leng Y, Nazir F, et al. Mixed convection phenomenon for hybrid nanofluid flow exterior to a vertical spinning cylinder with binary chemical reaction and activation energy. *Case Stud Therm Eng* 2024; 54: 103943.
25. Mahmud MZ and Molla MM. Natural convection and heat transmission of two-phase Bingham Fe3O4-CoFe2O4-water hybrid nanofluid flow in an enclosure with a corrugated heated cylinder. *Phys Scr* 2024; 99(6): 065267.
26. Akbar NS, Akram J, Hussain MF, et al. Thermal storage study and enhancement of heat transfer through hybrid Jeffrey nanofluid flow in ducts under peristaltic motion with entropy generation. *Therm Sci Eng Prog* 2024; 49: 102463.
27. Akbar NS, Akram J, Fiaz Hussain M, et al. Hybrid nanofluid flow and heat transfer in symmetric porous ducts with CuO nanoparticles and multi-walled carbon nanotubes under peristaltic motion. *Mod Phys Lett B* 2024; 38(33): 2450333.
28. Ghadikolaei SS and Gholinia M. Terrific effect of H2 on 3D free convection MHD flow of C2H6O2H2O hybrid base fluid to dissolve Cu nanoparticles in a porous space considering the thermal radiation and nanoparticle shapes effects. *Int J Hydrogen Energy* 2019; 44(31): 17072–17083.
29. Ghadikolaei SS and Gholinia M. 3D mixed convection MHD flow of GO-MoS2 hybrid nanoparticles in H2O–(CH2OH)2 hybrid base fluid under the effect of H2 bond. *Int Commun Heat Mass Transf* 2020; 110: 104371.
30. Ghadikolaei SS, Gholinia M, Hoseini ME, et al. Natural convection MHD flow due to MoS2–Ag nanoparticles suspended in C2H6O2H2O hybrid base fluid with thermal radiation. *J Taiwan Inst Chem Eng* 2019; 97: 12–23.
31. Fadhel MA, Asghar A, Lund LA, et al. Dual numerical solutions of Casson SA–hybrid nanofluid toward a stagnation point flow over stretching/shrinking cylinder. *Nanotechnol Rev* 2024; 13(1): 20230191.
32. Chaudhary MA and Merkin JH. Homogeneous-heterogeneous reactions in boundary-layer flow: effects of loss of reactant. *Math Comput Model* 1996; 24(3): 21–28.
33. Khan MI, Hayat T, Khan MI, et al. A modified homogeneous-heterogeneous reactions for MHD stagnation flow with viscous dissipation and Joule heating. *Int J Heat Mass Transf* 2017; 113: 310–317.
34. Hussain Z, Hayat T, Alsaedi A, et al. On MHD convective flow of Williamson fluid with homogeneous-heterogeneous reactions: A comparative study of sheet and cylinder. *Int Commun Heat Mass Transf* 2021; 120: 105060.
35. Ramzan M, Bilal M and Chung JD. Effects of MHD homogeneous-heterogeneous reactions on third grade fluid flow with Cattaneo-Christov heat flux. *J Mol Liq* 2016; 223: 1284–1290.
36. He JH, Moatimid GM, Mohamed MA, et al. Unsteady MHD flow in a rotating annular region with homogeneous–heterogeneous chemical reactions of Walters' B fluids: Time-periodic boundary criteria. *Int J Mod Phys B* 2024; 38(14): 2450169.
37. Nandkeolyar M, Sarkar A, Sahu B, et al. Implications of homogeneous–heterogeneous reactions, Hall current, and dissipative radiative heat transfer on MHD Casson fluid flow over a bi-directional stretching sheet. *Numer Heat Transf A Appl* 2024; 1–18. DOI: 10.1080/10407782.2024.2360660
38. Tanveer A, Jarral S and Saleem S. Dynamic interactions in MHD Jeffrey fluid: Exploring peristalsis, electro osmosis and homogeneous/heterogeneous chemical reactions. *Alex Eng J* 2024; 94: 354–365.
39. Pooja MN, Narasimhamurthy SK and Anitha V. Numerical investigation of flow dynamics of Williamson fluid over an expanding cylinder/plate in presence of homogeneous/heterogeneous reactions. *Int J Appl Comput Math* 2024; 10(1): 10.
40. Ramzan M, Chaudhry H, Ghazwani HAS, et al. Impact of homogeneous–heterogeneous reactions on nanofluid flow through a porous channel – a Tiwari and Das model application. *Numer Heat Transf A Appl* 2024; 85(8): 1317–1330.
41. Noor S. Homogeneous–heterogeneous reactions in the colloidal investigation of Casson fluid. *Open Phys* 2024; 22(1): 20230174.
42. Hamilton RL and Crosser OK. Thermal conductivity of heterogeneous two-component systems. *Ind Eng Chem Fundam* 1962; 1(3): 187–191.
43. Khan MN, Ahammad NA, Ahmad S, et al. Thermophysical features of Ellis hybrid nanofluid flow with surface-catalyzed reaction and irreversibility analysis subjected to porous cylindrical surface. *Front Phys* 2022; 10: 986501.
44. Veera Krishna M. Hall and ion slip effects on MHD laminar flow of an elastico-viscous (Walter's-B) fluid. *Heat Transf* 2020; 49(4): 2311–2329.
45. Alarabi TH, Rashad AM and Mahdy A. Homogeneous–heterogeneous chemical reactions of radiation hybrid nanofluid flow on a cylinder with joule heating: Nanoparticles shape impact. *Coatings* 2021; 11(12): 1490.
46. Vatani A, Woodfield PL and Dao DV. A survey of practical equations for prediction of effective thermal conductivity of spherical-particle nanofluids. *J Mol Liq* 2015; 211: 712–733.

47. Gul H, Ramzan M, Nisar KS, et al. Performance-based comparison of Yamada–Ota and Hamilton–Crosser hybrid nanofluid flow models with magnetic dipole impact past a stretched surface. *Sci Rep* 2022; 12(1): 29.
48. Alwawi FA, Alkasasbeh HT, Rashad AM, et al. A numerical approach for the heat transfer flow of carboxymethyl cellulose-water based Casson nanofluid from a solid sphere generated by mixed convection under the influence of Lorentz force. *Mathematics* 2020; 8(7): 1094.
49. Zeeshan KI, Weera W and Mohamed A. Heat transfer analysis of Cu and Al2O3 dispersed in ethylene glycol as a base fluid over a stretchable permeable sheet of MHD thin-film flow. *Sci Rep* 2022; 12(1): 8878.
50. Sarma N and Paul A. Engine oil blended Casson hybrid nanofluid flow along a uniformly heated curved surface with Arrhenius activation energy and suction: a computational study. *Hybrid Adv* 2024; 5: 100161.
51. Ramesh GK, Manjunatha S, Roopa GS, et al. Hybrid (ND-Co3O4/EG) nanoliquid through a permeable cylinder under homogeneous-heterogeneous reactions and slip effects. *J Therm Anal Calorim* 2021; 146(3): 1347–1357.

Appendix

Notation

k	Permeability of the medium (m)
k_p	Porosity parameter
n	Exponential index
p	Pressure (Pa)
$\mathbf{q}^*$	Velocity vector (ms^{-1})
q_e	Heat flux at the surface ($W/m^)$
u_r, u_θ, u_z	Velocities corresponding to the radial, azimuthal, and axial directions (ms^{-1})
A	Concentration of species α_c (mol/m)
B	Concentration of species β_c (mol/m)
B_0	Applied magnetic field strength (T)
C_F	Skin friction coefficient
D_A, D_B	Diffusion coefficients for species α_c and β_c (m/s)
$\mathbf{E_i}$	Electric field (V/m)
Ec	Eckert number
H_c	Hall parameter
H_i	Ion-slip parameter
$\mathbf{I}$	Identity tensor
$\mathbf{J}_0, \mathbf{J_i}$	Current density (A/m)
K	Thermal conductivity ($Wm^{-1}K^{-1}$)
K_c, K_s	Rate constant for homogeneous & heterogeneous reaction (m/mol·s)
K_{vs}	Strength of homogeneous-heterogeneous reaction due to slip
M	Magnetic parameter
Nu	Local Nusselt number
Pr	Prandtl number
Q_u, Q_0, Q_e	Uniform heat source, Space-dependent heat source, and Heat source coefficient (W/m^2)
R_{hom}, R_{het}	Rate of homogeneous & heterogeneous reaction (mol/m·s)
Sc	Schmidt number
S_u	Suction parameter
S_1	Thermal-dependent heat source parameter
S_2	Exponential space-dependent heat source parameter
T	Temperature of fluid (K)
T_w	Wall temperature (K)
T_∞	Ambient temperature (K)
U_w, U_0	Wall velocity at the cylinder surface and Reference velocity (ms^{-1})
$\mathbf{V_i}$	Ion velocity (m/s)
V_w	Wall suction velocity (m/s)
We	Weissenberg number
α	Thermal diffusivity (m/s)
α_1	Slip coefficient for velocity (m)
α_2	Slip coefficient for temperature (K/m)
β^*	Ratio of diffusion coefficients D_B/D_A
γ	Curvature parameter
γ^*	Shear rate function (s^{-1})
δ_1	Dimensionless velocity slip parameter
δ_2	Dimensionless thermal slip parameter
δ_3	Homogeneous-heterogeneous reaction parameter
Γ	Williamson's fluid parameter
ρ	Fluid density (kgm^{-3})
σ	Electrical conductivity (Sm^{-1})
ω_c	Cyclotron frequency (Hz)
φ	Volume fraction
μ	Dynamic viscosity (Pas^{-1})
μ_∞	viscosity at infinite shear stress (Pas^{-1})
ν	Kinematic viscosity (m^2s^{-1})
τ_c	Collision time (s)
τ_e	Extra stress
τ_{rz}	Shear stress in the $r-z$ direction (N/m)
τ_0	Total stress tensor (Pa)
ζ	Similarity variable
∇	Gradient operator (m^{-1})
$\boldsymbol{\alpha}_1$	Rate of strain tensor (s^{-1})
$\boldsymbol{\Gamma}$	Positive time constant (s)
Π	Second invariant of the strain rate tensor (s^{-2})